AIAA JOURNAL
Vol. 50, No. 12, December 2012

Toward Designing with Three-Dimensional Bumps for Lift/Drag Improvement and Buffet Alleviation

Jeremy P. Eastwood* and Jerome P. Jarrett†
University of Cambridge, Cambridge, England CB2 1PZ, United Kingdom

DOI: 10.2514/1.J051740

The desire to design more efficient transport aircraft has led to many different attempts to minimize drag. One approach is the use of three-dimensional shock control bumps, which have gained popularity in the research community as simple, efficient and robust devices capable of reducing the wave drag of transonic wings. This paper presents a computational study of the performance of three-dimensional bumps, relating key bump design variables to the overall wing aerodynamic performance. An efficient parameterization scheme allows three-dimensional bumps to be directly compared to two-dimensional designs, indicating that two-dimensional bumps are capable of greater design point aerodynamic performance in the transonic regime. An advantage of three-dimensional bumps lies in the production of streamwise vortices, such that, while two-dimensional bumps are capable of superior performance near the design point, three-dimensional bumps are capable of breaking up regions of separated flow at high Mach numbers, suggesting improvement in terms of buffet margin. A range of bump designs are developed that exhibit a tradeoff between design point aerodynamic efficiency and improvement in buffet margin, indicating the potential for bespoke designs to be generated for different sections of a wing based on its flow characteristics.

Nomenclature

b_{edge}	=	spanwise three-dimensional SCB shoulder width
b_{spacing}	=	spanwise three-dimensional SCB spacing
b_{width}	=	spanwise three-dimensional SCB width
c	=	section chord
C_D	=	drag coefficient
C_L	=	lift coefficient
c_p	=	pressure coefficient
l_{ramp}	=	streamwise length of SCB ramp
l_{tail}	=	streamwise length of SCB tail
M	=	local Mach number
M_{sh}	=	shock upstream Mach number at boundary layer edge
M_∞	=	freestream Mach number
p	=	static pressure
p_0	=	stagnation pressure
Re	=	Reynolds number
$V_{x,y,z}$	=	x, y, z components of velocity vector
$\boldsymbol{V}_{xz}$	=	velocity vector in x-z plane
x_{shock}	=	streamwise normal shockwave location
x_{start}	=	streamwise starting location of SCB
x'	=	optimal SCB design vector
α	=	angle of attack
ΔMx	=	change in buffet onset prediction from correlation x over clean wing value
θ_{ramp}	=	SCB ramp angle relative to local wing surface
$\theta_{\text{ramp,max}\,L/D}$	=	θ_{ramp} achieving maximum L/D for a given spanwise SCB design
τ_{wx}	=	wall shear stress measured in the chordwise direction
Φ	=	SCB isolation ratio
ω	=	vorticity vector
ω_{str}	=	measure of streamwise vorticity

Presented at the 49th AIAA Aerospace Sciences Meeting, Orlando, FL, January 4–7, 2011; received 14 November 2011; revision received 22 March 2012; accepted for publication 15 April 2012.

*Ph.D. Candidate, Department of Engineering, Trumpington Street. Student Member AIAA.

†University Lecturer, Department of Engineering, Trumpington Street. Member AIAA.

I. Introduction

INCREASING awareness of the environmental impact of our actions today has led to a shift in priorities for designers in many disciplines. Particular attention has been paid to air travel and the long-term implications of emitting CO_2 and other combustion products directly into the high-level atmosphere. This growing environmental pressure, coupled with the economic drive to reduce operating costs, places increasing demands on the commercial aircraft designer to develop ever-more efficient airliners. At the center of this drive for efficiency is aircraft drag reduction.

One method of reducing drag in the transonic regime is through the use of small bumps on the wing surface to break up local supersonic shock waves into lower entropy-creating systems. Although earlier investigations [1] considered shock control bumps (SCBs) as a method of improving off-design transonic aerofoil performance (in particular, drag divergence and buffet) by fixing shock location, Ashill et al. [2] were the first to consider SCBs purely as a method for wave drag reduction. Their SCB design was a variable-height device with a shape formed via deflection of a flexible plate; wave drag reduction was achieved by reducing the original normal shock strength via a series of compression waves introduced by the concave upstream flank of the SCB.

A number of two-dimensional SCB studies [3,4] have since indicated that their performance is governed by only a few key design variables, namely, crest height and location relative to the original normal shock wave. A wedge-shaped SCB design with linear ramp and tail sections emerged as an alternative to the original bent-beam shape; the curvature discontinuity at the ramp foot creates an oblique shock that interacts with the normal shock to produce a λ-shock system, as shown in Fig. 1. Not only does this design generate almost identical drag reductions as the bent-beam-shaped SCB despite the differences in flow physics of the interaction [3], but it was shown by König et al. [5] to provide a more robust performance under off-design conditions by fixing the front leg of the λ-shock system. Ogawa and Babinsky [6] presented an analytical study of the λ-shock interaction, linking SCB performance to an "effective flow turning angle" over the upstream ramp of the SCB (explicitly defined by the wedge ramp angle for the two-dimensional wedge-shaped SCB). The

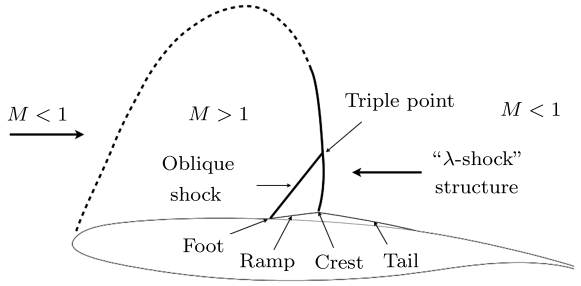

Fig. 1 Diagram of λ-shock system produced by an SCB on a transonic wing.

study also identified mechanisms of SCB performance breakdown: incorrect SCB streamwise placement relative to the original normal shock wave leads to unwanted flow reexpansions and stronger shock waves, and excessive flow turning angles over the upstream ramp of the SCB can lead to a sudden breakdown of the λ-shock structure. This rapid performance degradation of two-dimensional SCBs under off-design conditions has often pushed researchers into considering SCBs as adaptive devices [7], thereby reducing their potential advantages over other drag reduction technologies in terms of simplicity, weight, and ease of retrofit.

Initial three-dimensional SCB studies considered spanwise extrusions of two-dimensional SCBs on infinite swept wings [8,9] and isolated finite span bumps in oblique flow [10]. Closely spaced three-dimensional SCB arrays were first considered in an experimental study by Holden and Babinsky [11] as an alternative to three-dimensional arrays of passive devices such as slots and grooves. They showed that the λ-shock structure created by their wedge-shaped three-dimensional SCBs extended further spanwise than the SCB itself; with the correct spanwise spacing, an array of three-dimensional SCBs could therefore produce an almost two-dimensional control effect. A further finding was that three-dimensional SCBs produced pairs of streamwise vortices, potentially capable of delaying downstream separation, and thus beneficial off-design. These findings have been confirmed by a number of subsequent experimental [12–15] and numerical [16,17] studies. The potential for similar on-design performance of three-dimensional SCB arrays compared with two-dimensional SCBs with improved off-design performance has led to them being considered as an attractive alternative to dynamic two-dimensional devices [18].

Although two-dimensional SCB performance on- and off-design has been linked to key design variables, this is not the case for three-dimensional SCBs. For three-dimensional SCBs, the effective flow turning angle is less than the geometric SCB design [6,11,15], and overall array performance will depend on spanwise SCB spacing, which dictates the degree of pseudoconical λ-shock overlap. To be able to effectively design with three-dimensional SCBs, a better understanding of the relationship between key design variables and overall performance, as well as of the tradeoff between two-dimensional and three-dimensional performance, is required. This paper will use parametric studies to relate the performance of three-dimensional SCB arrays to their key design variables on an infinite span wing section, as well as compare their on- and off-design performance with that of two-dimensional SCBs.

The paper first describes the SCB parameterization and computational model used for the analyses, then presents and discusses the design point parametric investigations of aerodynamic performance followed by vortex identification and strength comparisons for select SCB designs, and the link between vortex strength and buffet alleviation. Finally, the trade-off between design point performance and buffet alleviation is examined and the governing design variables discussed, before the paper is concluded.

II. Model Setup

The ideal test bed for parametric studies with three-dimensional SCB arrays would be a full aircraft wing-body model, such as the DLR-F4 [19] or NASA CRM [20] (alternative simple transonic aircraft designs developed to provide models for computational and experimental comparison, and CFD validation). However, because of computational resource limitations, full aircraft simulations are infeasibly expensive for the number of analyses required in the present study [$O(10^2)$]. To reduce simulation time, an infinite wing model with a three-dimensional SCB array was created using a finite wing section with symmetry boundary conditions. The aerofoil used was the DFVLR-R4, a turbulent transonic design with a finite trailing edge (TE) thickness of $0.005c$, which is used for the DLR-F4 outer wing section [21]. For the analyses undertaken thus far, only flow perpendicular to the wing leading edge (LE) was considered, with $M_\infty = 0.705$ and $\alpha = 0^\circ$ in all cases presented. These values were chosen to provide a M_∞ comparable to the cruise value for the DLR-F4, taking into account quasi-three-dimensional wing sweep effects, while producing a reasonable-strength shock wave ($M_{\text{sh}} \simeq 1.3$, which is similar in strength to that used in several experimental SCB investigations [11,12,15]) around the midchord point of the aerofoil (see Fig. 2). The Reynolds number was set to $Re = 3 \times 10^6$ for comparison with studies performed on the DLR-F4 [19], leading to a clean-wing performance of $C_L = 0.97$, $C_D = 0.0241$ and $L/D = 40.2$ (based on computational fluid dynamics (CFD) analysis of the wing section using the solver described in Sec. II.B). The lift and drag of the wing section were calculated through a surface integration of pressure and friction forces, limiting the ability for wave drag determination through drag decomposition; however, analysis of the DFVLR-R4 aerofoil by the two-dimensional potential flow coupled boundary-layer solver VGK (incorporating shock models) [22] estimated the wave drag to account for 40% of the total drag at the chosen design point.

A. SCB Geometry

The overall geometry of the wing section with three-dimensional SCB is shown in Fig. 3. The streamwise SCB profile was chosen to have a wedge shape, as shown in Fig. 3b. Thus, θ_{ramp} provides explicit control over the flow turning angle, one of the key SCB design parameters. Variables l_{ramp} and l_{tail} were fixed at $0.1c$ and $0.2c$, respectively, for all parametric studies. The variable l_{ramp} was chosen as a typical value based on existing studies [6], and l_{tail} was set as a compromise between reducing the flow turning angle over the bump crest and minimizing the wetted area of the three-dimensional SCB. Although likely to affect SCB performance, they were kept fixed to concentrate on the more important spanwise variables. Fixing l_{ramp} coupled the SCB height with θ_{ramp} in the investigations. Although the SCB height has been observed to be a key design feature [2,4], θ_{ramp} was shown to have a more direct influence over the control strength [6] and so was used as the sole streamwise design variable; a decoupling of the SCB height and θ_{ramp} through variation of l_{ramp} could not be explored in the time frame of the investigations. The SCB is defined relative to the original aerofoil surface, i.e., the ramp

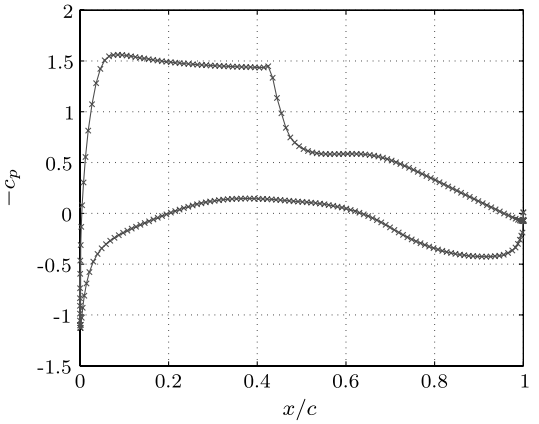

Fig. 2 Distribution of c_p over clean wing section at design point from Fluent CFD analysis.

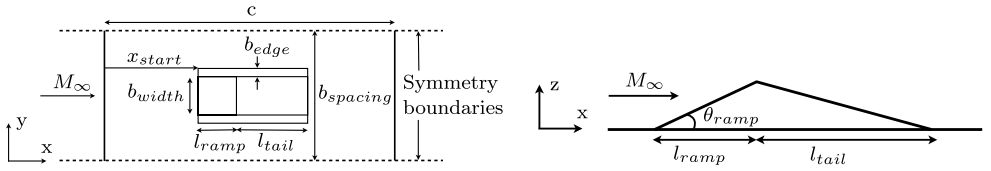

a) Planform view of 3D SCB geometry

b) Streamwise view of 3D SCB geometry (shown relative to flat plate for clarity)

Fig. 3 Three-dimensional SCB geometry and parameter definitions.

shape is conformally added to the original aerofoil coordinates, so that it thus inherits the curvature of the underlying aerofoil. This means that θ_{ramp} is the exact geometrical turning angle at the start of the bump relative to the original aerofoil surface, giving direct control over the flow turning and ensuring it remains constant, independent of where the bump is placed on the aerofoil; an additional benefit is that $\theta = 0°$ reproduces the original, clean aerofoil.

The spanwise three-dimensional SCB geometry is defined in Fig. 3a; the model span defines the spanwise SCB spacing, b_{spacing}. Although there are clearly many more options for planform design of three-dimensional bumps, this simple approach was chosen to investigate the relative importance of the key global parameters. The shoulder regions are a linear lofting between the clean aerofoil surface and raised bump profile, thus introducing discontinuities in the surface spanwise gradient. It is possible that these discontinuities could lead to sub-optimal SCB performance for a given spanwise design; however, because of the limitations on spanwise mesh spacing for the computational model (discussed in Sec. II.C), a more sophisticated shoulder design could not be accurately represented. Because of the limited number of variables considered, the spanwise SCB design was held constant along the SCB length; although it is anticipated that more detailed shape variations could yield performance benefits, the time frame and computational resources available for the investigations limited design exploration to these few key features. Two-dimensional SCBs were investigated by setting $b_{\text{width}} = b_{\text{spacing}}$ with $b_{\text{edge}} = 0$.

B. CFD Solver Settings

CFD analysis was performed using ANSYS Fluent version 12.1.2, using the density-based-implicit solver [23], with second-order upwind schemes used to discretize the governing equations and far-field pressure conditions applied at the streamwise boundaries. The Spalart–Allmaras (S-A) turbulence closure model was used, again with second-order discretization. The S-A turbulence model was chosen because it only requires a single additional equation for its solution at each iteration (reducing the overall simulation time over that of more complicated multi-equation models), and it is designed specifically for wall-bounded external flows in aerospace applications and, as such, has been shown to produce excellent flow predictions, even outperforming many of its two-equation alternatives [24]. Although the S-A model is expected to provide an accurate prediction of flow behavior over the wing during normal operating conditions, and even under influence of a shock [25], its representation of post-separation flow behavior and flow reattachment is expected to be poor [24–26]. Despite some improvements in postseparation modeling with alternative two-equation models (e.g., shear-stress transport k-ω), no model is likely to be able to accurately predict boundary-layer reattachment essential to modeling shock-induced separation bubbles [24], and so it was decided that the additional expense associated with the two-equation models outweighed the benefits they offered. The Courant number was increased to 20 during calculations to speed up convergence.

C. CFD Model

A simple O-H grid was generated using the meshing software IcemCFD. The O grid attached to the wing surface allowed close control over the boundary-layer mesh (see Fig. 4a). A total of 120 nodes were used chordwise over the wing surface, with LE and TE spacings set at $0.2\%c$, and a maximum chordwise spacing of $1\%c$. The first cell height was set to give $1 \leq y^+ \leq 4$ over the entire wing section (this complies with the Fluent meshing guidelines for the S-A turbulence model, which recommends $y^+ < 5$ over the surface to correctly model the viscous sublayer [23]), with the O grid extending 15 nodes in the surface-normal direction. The solution domain

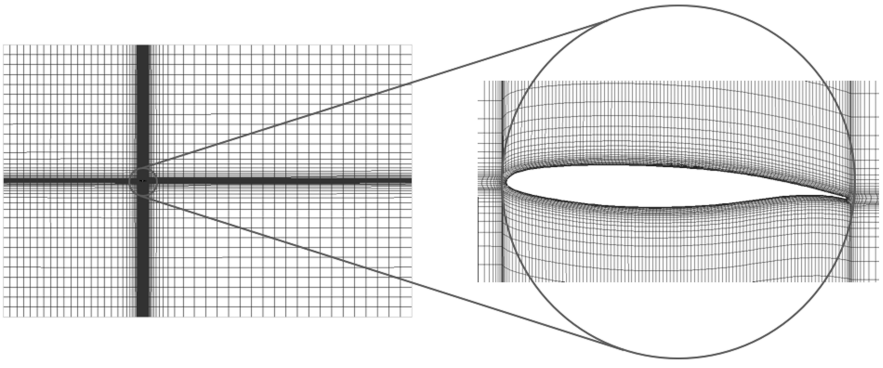

a) Mesh in streamwise plane

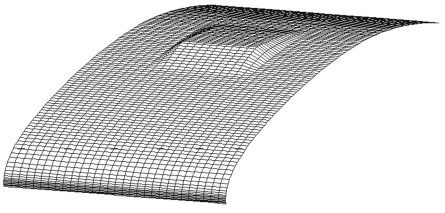

b) Mesh over wing upper surface with 3D SCB

Fig. 4 O-H mesh used for simulations.

extended $20c$ upstream, above and below the wing section, and $40c$ downstream; although this domain extension is on the acceptable limit for simulation of a lifting wing section [23], the value was chosen to keep mesh size to a minimum, reducing the computational burden of the CFD analyses. A spanwise node spacing of $1\%c$ was used for all cases, ensuring the geometry is properly captured (see Fig. 4b) while keeping the number of cells as low as possible to aid solution time. The overall mesh size varied from 410,000 to 1.71 million cells, depending on the spanwise bump spacing. The mesh resolution was coarser than that used in other numerical studies on three-dimensional SCBs [14,17]; however, the computational resources available and large number of alternative designs being considered in the study put practical limitations on the size of the model mesh and, therefore, on the grid resolution.

To speed up the parametric studies, each case was analyzed in parallel over eight 2.33-GHz CPUs, sharing a total of 4 GB of RAM (a practical limit for mesh size was 2 million cells, based on the implicit solver settings and available RAM). Initial studies indicated that 3200 iterations were required for convergence of the lift and drag forces over the wing section, with a corresponding solution wall-clock time of 3 h. Because of licensing limitations, only one case could be analyzed at a time.

To assess the accuracy of the simulation, CFD predictions of surface c_p over the clean aerofoil using both the standard mesh (outlined previously) and a fine mesh were compared to experimental data from tests in the NASA Langley transonic cryogenic wind tunnel conducted in 1984 [27]. The fine mesh was obtained by doubling the chordwise node spacing and increasing the number of nodes in the boundary layer O grid to 23, resulting in a solution with $y^+ \simeq 1$ over the entire surface. The flow conditions for the comparison are the closest available in the experimental tests to the chosen operating point for the parametric studies. The comparison is presented in Fig. 5. Because of the increased cost of the fine mesh simulations with no significant benefit, the standard mesh was deemed sufficient for the SCB investigations.

To assess the accuracy of the spanwise mesh spacing, the wing section was analyzed with a three-dimensional SCB ($b_{\text{spacing}} = 0.3c$, $b_{\text{width}} = 0.1c$, $b_{\text{edge}} = 0.02c$, $\theta_{\text{ramp}} = 6°$) attached. As no experimental data were available for comparison, a grid resolution study was performed by multiplying the spanwise mesh spacing by a factor of $1/2^n$, with $n = -1, 0, 1, 2, 3$ ($n = 3$ represents the largest mesh size that could be run using the chosen flow solver settings and computational resources available), and comparing the L/D predictions, with the other mesh details fixed at the values described previously. The L/D predictions for each model are plotted against the mesh size (halving the spanwise spacing doubled the mesh size) in Fig. 6, indicating that although the datum mesh (that with a size of 0.5×10^6 cells) does not provide a mesh-independent solution, the differences from the finest mesh designs are 0.6% or less. The datum mesh thus represents a good compromise between accuracy and a expense.

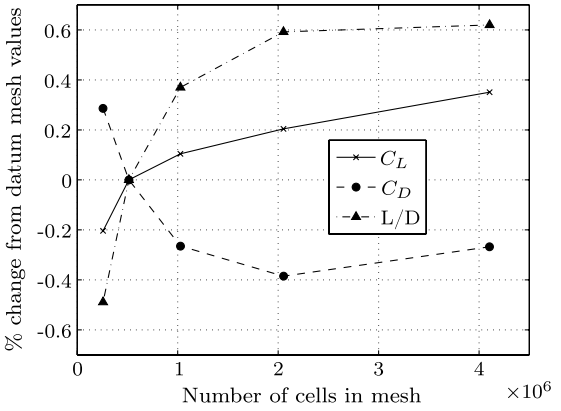

Fig. 6 Force predictions over DVLR-F4 aerofoil with three-dimensional SCB at design point for model with variable spanwise mesh spacing.

Although Fig. 6 shows that increasing the spanwise grid resolution would change the model force predictions, potentially improving its accuracy, the mesh was designed so that the exact same spacing was used for all SCB designs, suggesting that errors due to the chosen mesh resolution would be similar between different models, allowing their comparative benefits to be assessed fairly. The ability of the chosen mesh to predict the aerodynamic forces over the wing section was invstigated by comparing the C_L and C_D prediction over the clean DVLR-F4 aerofoil from the chosen numerical model with experimental data from wind tunnel tests performed in the NASA Langley transonic cryogenic wind tunnel in 1984 [27]. Figure 7 presents a comparison between the drag polars predicted by CFD and experiment, obtained by varying α at a fixed M_∞ and Re, which were selected to be as close to the chosen design point for the SCB parametric studies as possible. Figure 7 indicates that, despite an overprediction in C_D at low C_L, the drag rise is predicted well up to just above $C_L = 1$. Above this point, the trends between the experimental and computational drag polars differ, indicating that the model provides a less adequate representation of the flow behavior in this range. This is likely to be due to inaccuracies associated with post-separation flow modeling (shock separation first appears at $C_L \simeq 1$ and, at the highest C_L condition analyzed, it extends fully from the shock to section TE). CFD simulations with the chosen mesh are therefore considered to provide accurate representations of the transonic flow over the wing section at the design point chosen for the SCB investigations.

III. Results and Discussion

A. Variable SCB Spanwise Parameters

Variations in overall wing L/D were calculated at the design point flow conditions (fixed α) for SCB designs with variable b_{spacing} and

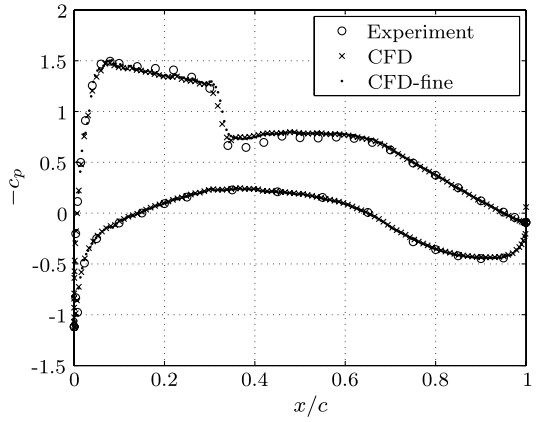

Fig. 5 Distribution of c_p over DFVLR-F4 aerofoil at $Re = 4 \times 10^6$, $M_\infty = 0.7$, $C_L = 0.825$.

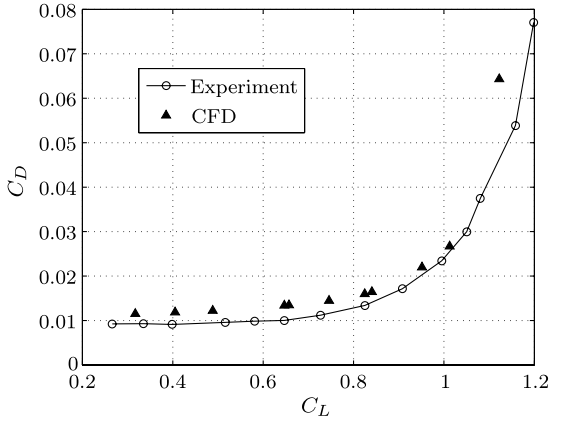

Fig. 7 Force predictions over DVLR-F4 aerofoil with $M_\infty = 0.7$, $Re = 4 \times 10^6$, variable α.

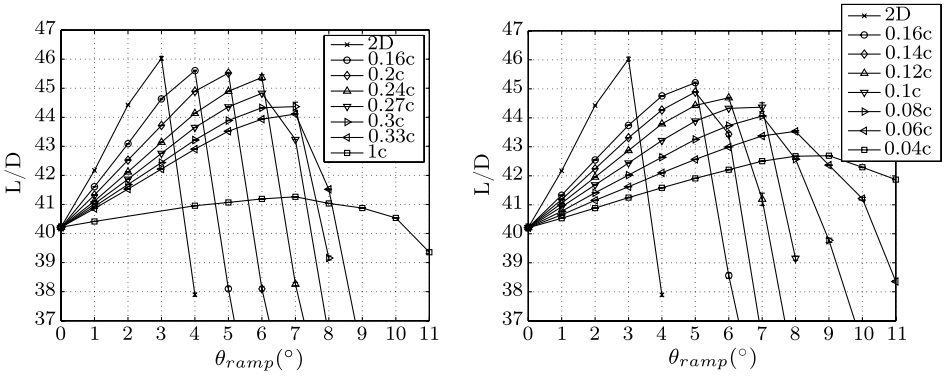

a) Variable $b_{spacing}$ and θ_{ramp}; b_{width} = 0.1 **b) Variable b_{width} and θ_{ramp}; $b_{spacing}$ = 0.3c**

Fig. 8 L/D performance for three-dimensional SCB designs with variable θ_{ramp}.

fixed b_{width} and are shown in Fig. 8a; those obtained by varying b_{width} with fixed $b_{\text{spacing}} = 0.3c$ are shown in Fig. 8b. For each combination of b_{spacing} and b_{width}, θ_{ramp} was varied upward from 0° (the clean wing case); the two-dimensional SCB is shown as a limiting case in both studies, obtained when $b_{\text{spacing}} \leq b_{\text{width}}$. For all cases, $b_{\text{edge}} = 0.02c$, with the other parameters set as described previously. The variable x_{start} was also fixed at $0.39c$ (thus, a ramp peak location of $0.49c$) for all cases, based on a clean wing shock location of $x_{\text{shock}} \simeq 0.46c$ (see Fig. 2). The results in Fig. 8 (and in all subsequent figures displaying L/D) include (the small) convergence error bars based on variations in the calculated lift and drag over the last 200 iterations of each simulation. The measured L/D variations from the clean wing were caused by changes to both lift and drag forces on the wing section, meaning that the design point C_L varied between the different SCB designs analyzed. Analysis at constant C_L would require a variation of α between different SCB designs, leading to a possible change in shock location and strength and, thus, SCB performance. Therefore, although a reduction in C_L would be expected to generate a reduction in C_D for a clean wing section, the same is not necessarily true for a section with SCB fitted, and so the change to the relative L/D variation with SCB design for a constant C_L condition compared to that at constant α is not sraightforward. Although evaluation of section drag (or L/D) at a constant C_L would provide a more aerodynamically relevant metric for comparison between designs, this would require performing several flow simulations for each case (depending on the desired accuracy in C_L).

The reduction in maximum attainable L/D of three-dimensional SCBs with increased b_{spacing} and reduced b_{width} observed in Fig. 8 is partially due to the finite spanwise extent of the three-dimensional λ-shock system. This is highlighted by Fig. 9, which compares the gain in p_0 for the wing with SCB over the clean wing design (and is thus a measure of drag saving) in a spanwise plane $0.01c$ downstream of the end of the SCB tail for the two-dimensional SCB with $\theta_{\text{ramp}} = 3°$ and the three-dimensional SCB with $b_{\text{spacing}} = 0.3c$, $b_{\text{width}} = 0.1c$ and $\theta_{\text{ramp}} = 6°$. This indicates that, although the beneficial region (i.e., the three-dimensional λ-shock system) does extend further spanwise than the three-dimensional SCB itself (tying in with observations from other researchers [11–14,16,17]), its intensity is reduced. This suggests that, on-design, the two-dimensional SCB will always outperform a three-dimensional design, as the extruded two-dimensional λ-shock will always be able to cover more of the original normal shock wave than the three-dimensional λ-shock system, and thus be more effective as a drag reduction device. The strong variations seen at the bottom of Fig. 9b, i.e., large p_0 reductions over the SCB and large p_0 gains away from the SCB close to the surface, are due to slight variations in the height of the boundary layer just downstream of the SCB relative to the clean aerofoil case. They thus represent a local effect and do not translate to significant variations in global drag values.

Figure 10a shows the upper surface c_p contours for a typical three-dimensional SCB ($b_{\text{spacing}} = 0.3c$, $b_{\text{width}} = 0.1c$ and $\theta_{\text{ramp}} = 6°$), indicating the finite spanwise extent of the beneficial λ-shock system. This effect is quantified in Fig. 10b, which shows the spanwise variation of local section C_L, C_D, and L/D, obtained via surface integration of pressure and skin friction forces at different spanwise locations, highlighting the rapid local performance degradation in the spanwise direction away from the SCB. It also indicates that the L/D benefit of the SCB is due to a simultaneous C_D reduction and C_L increase. Figure 11 shows the variation of streamwise c_p distribution at different spanwise sections for the same three-dimensional SCB case along with those of the clean wing and the two-dimensional SCB from Fig. 9a for comparison, indicating the spanwise variation of control effectiveness. The relatively constant C_L increase across the model span seen in Fig. 10b is a consequence of the shock smearing produced by the SCB, which persists away from the three-dimensional SCB itself, reducing the

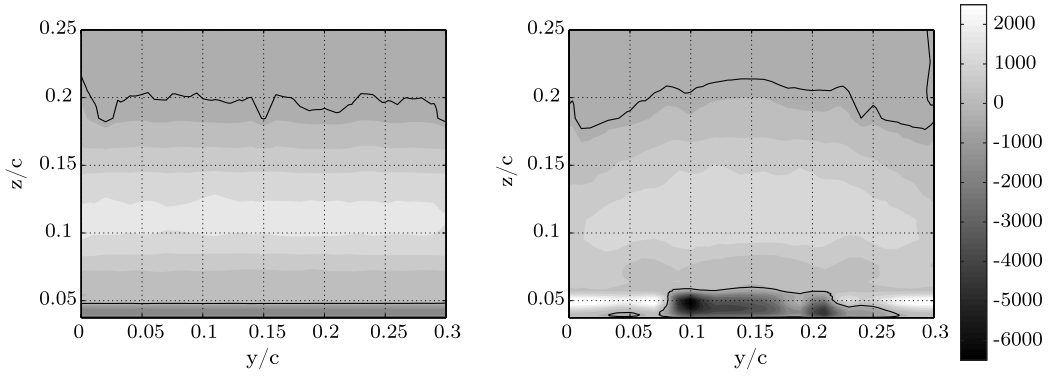

a) 2D SCB, θ_{ramp} = 3º **b) 3D SCB, θ_{ramp} = 6º**

Fig. 9 Contours of p_0 gain (N/m^2) over clean wing design over vertical spanwise plane at end of SCB for two-dimensional and three-dimensional SCBs; solid line marks zero gain.

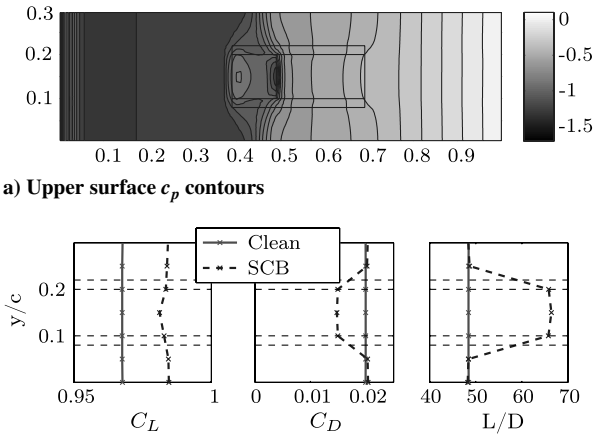

a) Upper surface c_p contours

b) Local section force integrals

Fig. 10 Three-dimensional SCB with $b_{\text{spacing}} = 0.3c$, $b_{\text{width}} = 0.1c$, and $\theta_{\text{ramp}} = 6°$.

immediate post-shock pressure rise, as shown in Figs. 11a and 11b, and increasing the section lift. The small reduction in C_L gain at the SCB centerline is due to the stronger compression over the SCB ramp in this region (see Fig. 10a) increasing the pressure over a larger streamwise section of the wing (see Fig. 11c); although this effect will be localized to the SCB ramp, the degree of isolation of this drop in C_L gain observed in Fig. 10b is likely to be a consequence of the number of spanwise measurement locations used.

A further observation from Fig. 8 is that the θ_{ramp} required to maximize L/D ($\theta_{\text{ramp,max}\,L/D}$) for three-dimensional SCB designs increases with both increasing b_{spacing} and decreasing b_{width}, i.e., as the three-dimensional SCB becomes more isolated. This has been summarized in Fig. 12, which plots the values of $\theta_{\text{ramp,max}\,L/D}$ for the designs in Fig. 8a against b_{spacing} Fig. 12a and the designs in Fig. 8b against b_{width} Fig. 12b, highlighting the observed trend. Both graphs show a linear increase in θ_{ramp} with three-dimensional SCB isolation; however, the departure from the trend for the highest b_{spacing} design in Fig. 12a indicates that this increase may be limited to a certain maximum value, depending on the other SCB spanwise variables. Exploration of this hypothesis and determination of this limiting value for different combinations of SCB spanwise design were not undertaken due to limitations on the time frame of the study. The more general trend of increased $\theta_{\text{ramp,max}\,L/D}$ with SCB isolation occurs because the effective flow turning angle (thus, strength of the leading leg of the λ-shock, and efficiency of the control) is reduced by spanwise flow leakage over the SCB ramp due to the spanwise pressure gradient (see Fig. 10a), as described by Ogawa [12] and Ogawa and Babinsky [6].

Figure 8 indicates that, for each SCB design, the L/D performance rapidly decreases away from the maximum value with increasing θ_{ramp}. The mechanism for this performance reduction is a breakdown of the λ-shock structure into a double-shock system, accompanied by strong flow reexpansion behind the SCB crest, as shown in Fig. 13 for the two-dimensional SCB. The double-shock system has a higher wave drag than the λ-shock structure (and the clean wing normal shock), and causes greater distress to the boundary layer, often leading to flow separation, which both increases drag and reduces lift. This breakdown is caused by the inability of the flowfield to support the triple point (required for the λ-shock structure shown in Fig. 1) compatible with the high flow turning angle specified by θ_{ramp} [6]. The same breakdown mechanism was observed for all the three-dimensional SCB designs studied in Fig. 8, with the final double-shock structure extending across the entire wing section (although the reexpansion region and thus strengthened secondary shock were localized to the SCB span). The severity of the performance reduction beyond the maximum is reduced for three-dimensional SCBs with greater b_{spacing} and smaller b_{width} (see Fig. 8) because of the reduced span of the flow reexpansion region, with the two-dimensional SCB exhibiting the most severe breakdown. The three-dimensional SCB design examined in Figs. 9–11, which is close to optimal (maximum L/D with respect to θ_{ramp} variation; see Fig. 8) exhibits localized flow reexpansion over the SCB crest (see Fig. 11c) while maintaining a λ-shock structure. This flow

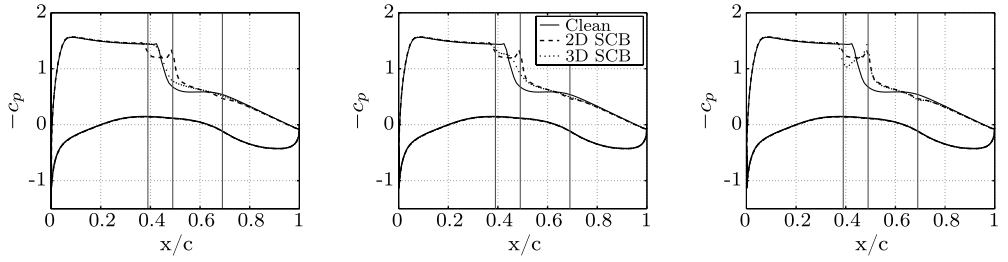

a) Midway between SCBs (y/c = 0) **b) Between symmetry plane and SCB centerline (y/c = 0.075)** **c) SCB centerline (y/c = 0.15)**

Fig. 11 Streamwise c_p distributions for three-dimensional SCB ($\theta_{\text{ramp}} = 6°$) compared to two-dimensional SCB ($\theta_{\text{ramp}} = 3°$) and clean wing; vertical lines mark SCB ramp, crest, and tail locations.

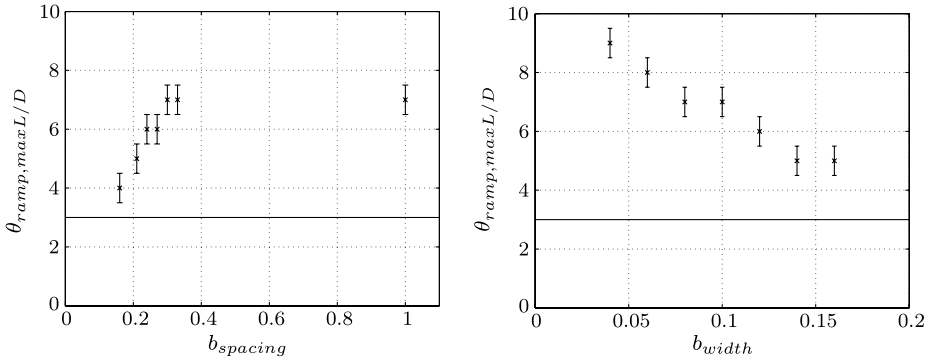

a) Variable $b_{spacing}$, $b_{width} = 0.1c$ **b) Variable b_{width}, $b_{spacing} = 0.3c$**

Fig. 12 Variation of $\theta_{\text{ramp,max}\,L/D}$ with spanwise variables for three-dimensional SCBs used in Fig. 8; solid line gives $\theta_{\text{ramp,max}\,L/D}$ for the two-dimensional SCB.

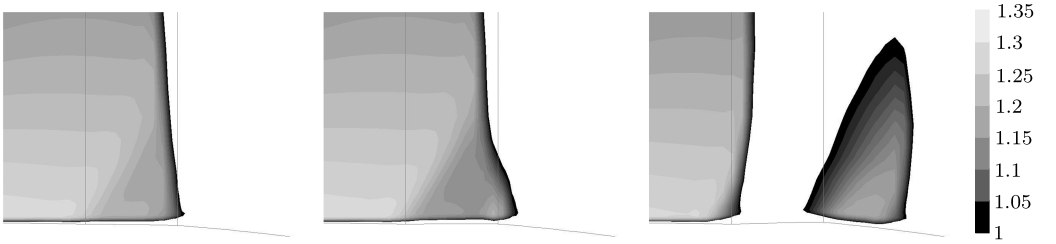

a) $\theta_{ramp} = 2^o$ b) $\theta_{ramp} = 3^o$ c) $\theta_{ramp} = 4^o$

Fig. 13 Supersonic Mach number contours over two-dimensional SCB designs with variable θ_{ramp}; vertical lines mark x_{start} and crest location.

reexpansion over the SCB crest at maximum L/D design is typical of the more isolated three-dimensional SCBs, with the effect diminishing as the designs move closer to the two-dimensional case (see Fig. 11c). Similar flow reacceleration over three-dimensional SCBs with high θ_{ramp} achieving high drag savings has been observed in experimental investigations performed at the University of Cambridge [12,13]. This suggests that the three-dimensional λ-shock structure is more resistant than the two-dimensional version to breakdown into the double-shock formation, enabling greater flow turning angles over the ramp and thus greater drag reductions for the flow close to the SCB, helping to balance out the regions of reduced savings between the SCBs. It is possible that three-dimensional SCB performance could therefore be improved by local modifications to the SCB crest design; however, it is not clear whether these potential improvements would enable superior design point performance to two-dimensional SCBs in the transonic regime.

B. Variable SCB Chordwise Location

The assumption of negligible difference of optimal x_{start} location for two- and three-dimensional SCBs was tested by varying x_{start} for two sample cases from the previous study (a two-dimensional SCB with $\theta_{ramp} = 3°$ and a three-dimensional SCB with $b_{spacing} = 0.3c$, $b_{width} = 0.1c$ and $\theta_{ramp} = 6°$), shown in Fig. 14. Although there is a small relative performance discrepancy between the two- and three-dimensional SCBs for different x_{start} values, the choice of fixing $x_{start} = 0.39c$ for all bump geometries should not unduly bias the results from the parametric studies. The optimal location of x_{start} has only been investigated for two SCB designs, and so it is possible that there is some variation of this value across the SCB design space; however, this was not investigated further due to limitations on the time frame for the study and the small performance variation between the two- and three-dimensional designs observed in Fig. 14.

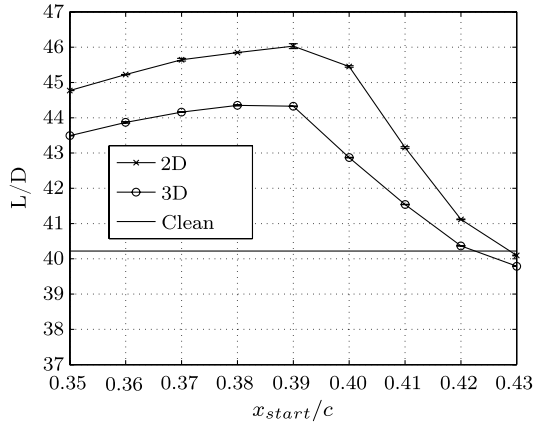

Fig. 14 L/D performance of two- and three-dimensional SCBs with variable x_{start}.

The drop in L/D away from $x_{start} = 0.39c$ is due to shock misalignment with the SCB crest for both two- and three-dimensional designs, reducing the L/D benefit of the device. For $x_{start} < 0.39c$ the rear leg of the λ structure sits downstream of the SCB crest; this allows the supersonic flow inside the λ-shock structure to be reexpanded over the crest, strengthening the λ-shock rear leg and increasing its associated drag, as shown in Fig. 15a. For $x_{start} > 0.39c$ the rear leg of the λ structure sits upstream of the SCB crest; the (high) subsonic flow behind the rear leg is accelerated to supersonic by the SCB ramp, which is then reexpanded over the crest, resulting in a secondary shock and thus increased drag, as shown in Fig. 15c. A similar variation of the flowfield over the centerline of three-dimensional SCBs has been observed in experimental investigations undertaken at the University of Cambridge for a flat-plate SCB model with variable shock location relative to the SCB crest [12,13,15].

C. Variable SCB Shoulder Design

Two studies were undertaken to assess the impact of varying b_{edge} on three-dimensional SCB performance. The first looked at varying b_{edge} while simultaneously varying b_{width} to hold the total SCB width $[b_{width} + (2 \times b_{edge})]$ constant, while the second looked at varying b_{edge} with b_{width} fixed. In both cases, b_{edge} was varied from $0c$ (vertical SCB sidewalls) to $0.05c$ in $0.01c$ intervals, and for each of these configurations, θ_{ramp} was increased from 0° in 1° intervals until a performance peak was found. The variations in L/D performance for the first and second studies are shown in Figs. 16a and 16b, respectively. The SCB designs with $b_{edge} = 0c$ required an alternative mesh to that used for all other SCBs, shown in Fig. 4; the SCB and wing surface grid was the same, but three additional evenly spaced grid lines were added along the vertical sidewalls to accurately mesh the model, with the lines originating from the point defined by the SCB ramp intersection with the clean wing, and

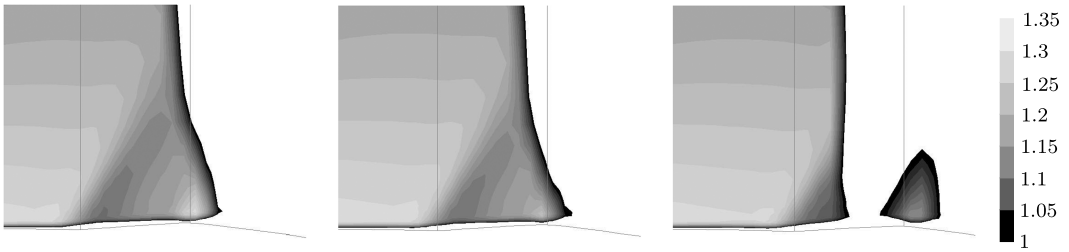

a) $x_{start} = 0.37c$ b) $x_{start} = 0.39c$ c) $x_{start} = 0.41c$

Fig. 15 Supersonic Mach number contours over plane down the center of three-dimensional SCB designs with variable x_{start}; vertical lines mark x_{start} and crest location.

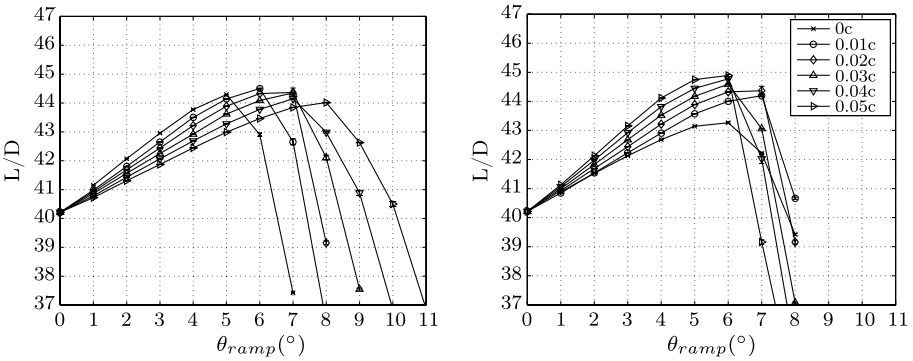

a) $b_{width} + (2 \times b_{edge}) = const. = 0.14c$ **b)** $b_{width} = const. = 0.1c$

Fig. 16 L/D variation with b_{edge}.

returning to the tail intersection with the wing. This generated several spanwise rows of triangular cells in the mesh; however, this did not lead to any convergence issues with the simulation.

Figure 16b indicates that increasing b_{edge} with b_{width} fixed improves L/D performance, because a greater spanwise extent of the flow is being directly affected by the SCB (its total width has increased). However, Fig. 16a indicates that, for $b_{\text{edge}} > 0.01c$, L/D performance decreases as b_{edge} becomes a greater proportion of the total SCB width. This is because the ramp angle seen by the flow passing over the shoulder regions at the front of the SCB is lower than that over the central ramp section and will therefore experience a lower degree of compression, a weaker λ-shock system, and thus a reduced p_0 saving. A reduction in the maximum achievable L/D is observed for the limiting case of $b_{\text{edge}} = 0c$ (see Fig. 16a, despite the fact that it performs better than all other designs at lower θ_{ramp}, suggesting that the λ-shock breakdown mechanism is not as stable for this design.

D. On-Design Performance Trends

Figures 8 and 16 indicate a reduction in attainable SCB performance (maximum achievable L/D) as the SCB becomes more isolated on the wing section (i.e., as it moves further from the two-dimensional design). By defining the SCB isolation ratio Φ as the gap between SCBs divided by the SCB spacing ($\Phi = 1 - (b_{\text{width}} + 2^{*} b_{\text{edge}})/b_{\text{spacing}}$), a clear relationship with the maximum achievable L/D with respect to θ_{ramp} emerges, as shown in Fig. 17a. A value of 1 for the isolation ratio describes a clean wing section (no SCB); however, a value of 0 does not explicity define a two-dimensional SCB (unless $b_{\text{edge}} = 0$); it is anticipated that a three-dimensional SCB with $b_{\text{edge}} > 0$ will have a slightly lower maximum L/D than the two-dimensional design due to the presence of finite shoulder sections. For simplicity, the two-dimensional SCB result has been given a value of 0. Each data set in Fig. 17a represents a separate parametric study undertaken: sets 1, 2, 4, and 5 correspond to Figs. 8a, 8b, 16a, and 16b, respectively, with sets 3 and 6 representing very similar studies undertaken to cover a fuller range in Φ. A cubic polynomial with an rms error of 0.256 has been fitted to the data in Fig. 17a using least squares; the small spread in the results indicates a strong dependence of L/D on Φ alone, and could be explained to some extent by prediction error (i.e., the 1° increments of θ_{ramp} used to find the maximum L/D for each design). The curve indicates a nonlinear performance degradation as the three-dimensional SCB becomes more isolated: the maximum achievable L/D drops 2% for isolation ratios up to 0.4, with a more rapid degradation beyond this point.

Although the isolation ratio best defines the effectiveness of the three-dimensional SCB in terms of maximum achievable L/D, θ_{ramp} at which this maximum is achieved ($\theta_{\text{ramp,max}\,L/D}$) is more closely correlated with the ratio $b_{\text{width}}/b_{\text{spacing}}$, shown in Fig. 17b, with a quadratic function (rms error = 0.496) providing a least-squares fit to the data. Increments of $\theta_{\text{ramp}} = 1°$ were used to find the maximum L/D point, explaining some of the spread in the data. Figure 17b indicates that θ_{ramp} at which the λ-shock over the center of the SCB breaks down into a double-shock system (which is correlated with $\theta_{\text{ramp,max}\,L/D}$; see Figs. 8 and 16) is goverened by the ratio of central SCB region (b_{width}) to b_{spacing}, as this defines the proportion of the flow being turned by the full θ_{ramp}. The variable dependencies shown in Fig. 17 are illustrated by Fig. 16: the designs in Fig. 16a have the same Φ and approximately the same maximum L/D with different $\theta_{\text{ramp,max}\,L/D}$, whereas the designs in Fig. 16b have the same $b_{\text{width}}/b_{\text{spacing}}$ ratio and have approximately the same $\theta_{\text{ramp,max}\,L/D}$ with a greater variation in maximum L/D.

The close least-squares fits of the data relating Φ to L/D_{max} and $b_{\text{width}}/b_{\text{spacing}}$ to $\theta_{\text{ramp,max}\,L/D}$ in Fig. 17 are good indicators of the dependence on these key parameters; however, it is likely that specific details of the cubic and quadratic functions used will vary with different operating conditions and underlying aerofoil design.

E. Off-Design Performance

Off-design performance of two families of SCBs were assessed by varying α, keeping M_∞ fixed. The L/D vs C_L performance for a

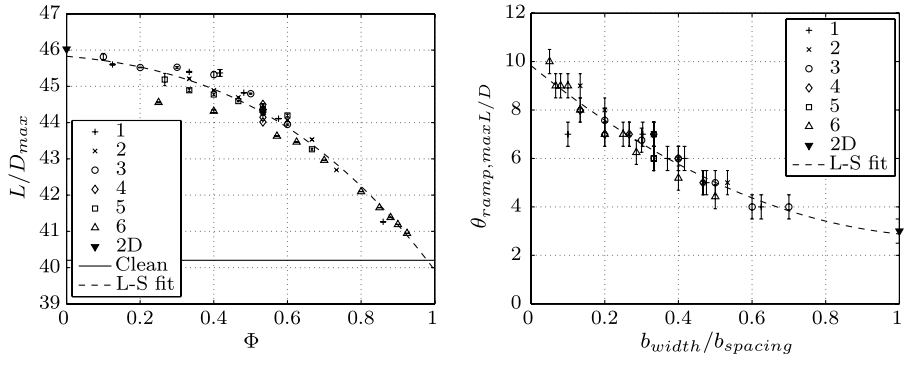

a) **b)**

Fig. 17 SCB performance variation with key design parameters.

family (variable θ_{ramp}) of two-dimensional SCBs is compared to that of a family of three-dimensional SCBs ($b_{\text{spacing}} = 0.3c$, $b_{\text{width}} = 0.1c$ and $b_{\text{edge}} = 0.02c$) in Fig. 18; for clarity, only selected designs from the three-dimensional SCB family are shown. For almost all designs, performance is seen to improve over that of the clean wing at C_L values higher than the design point (the points located in the range $0.97 \leq C_L \leq 1.0$ in Fig. 18, corresponding to $\alpha = 0°$), and degrades at C_L values below the design point, which is in agreement with findings from other two-dimensional [2,4] and three-dimensional [16] studies.

As the C_L of the wing section decreases, the shock wave decreases in strength and moves upstream; this movement is large enough to displace the shock wave entirely upstream of the SCB for all points below the design point C_L in Fig. 18, locating the SCB entirely in the subsonic flow. This shock misalignment leads to flow reacceleration over the SCB ramp and crest, terminated by a secondary shock, in the same mechanism seen in Fig. 15c. There is no λ-shock system as $x_{\text{shock}} < x_{\text{start}}$; thus, the SCB purely adds to overall wing drag, reducing the L/D as seen in Fig. 18. At C_L values above the design point, the shock moves downstream by 4–5%c on the clean wing, and increases in strength. Although the SCB restrains the shock movement to some extent by fixing the location of the λ-shock leading leg, the relative displacement of the clean wing shock location from the SCB crest leads to some movement of the λ-shock rear leg away from the SCB crest. This shock/crest misalignment also leads to flow reexpansion through the mechanism seen in Fig. 15a, and a strengthening of the λ-shock rear leg. Despite this, the λ-shock still generates a net reduction in drag, hence the L/D gain over the clean wing for most of the SCB designs in Fig. 18. The shock strengthening is greatest for SCB designs with the highest θ_{ramp} angles (which have the largest flow reexpansion over the crest) and most severe at high wing C_L conditions (x_{shock} is further downstream of the SCB crest, thus more of the shock wave is affected by the expansion waves coming off the crest). In the most severe cases considered (i.e., the SCBs with the highest θ_{ramp} values, analyzed at the highest C_L), this outweighs the benefit from the λ-shock structure, leading to an overall drag increase over the clean wing (see Fig. 18). This L/D performance reduction at C_L above the design point is contrary to findings from other SCB studies [2,4], which may be a consequence of greater shock movement relative to the SCB crest for these investigations at the highest C_L conditions, causing greater levels of unwanted flow reexpansion than in the existing studies. Although this could explain the discrepancy with existing SCB studies on laminar wing sections (due to their limited variation of shock location with operating conditions), the cause of the discrepancies is not as clear for studies on turbulent wing sections. Comparing two- and three-dimensional SCB designs that achieve a similar L/D at the design point ($C_L \simeq 0.97$), e.g., the 2° two-dimensional SCB and the 6° three-dimensional SCB in Fig. 18, indicates that the two-dimensional SCBs perform better at both high and low C_L off-design conditions. This is because the reduction in maximum achievable L/D for a three-dimensional SCB compared to a two-dimensional design implies that comparing SCBs with the same design point L/D requires the three-dimensional design to have not only a higher θ_{ramp}, but also a value closer (proportionally) to its specific value of $\theta_{\text{ramp,max}\,L/D}$. Therefore, despite the fact that three-dimensional λ-shock structures were observed previously to be more resilient to breakdown into double-shock systems with a given level of flow reexpansion, a three-dimensional SCB with the same design point L/D as a two-dimensional design will be closer to the point of serious flow reexpansion and λ-shock breakdown, and thus will experience more severe performance degradation when moving to off-design conditions.

Table 1 Freestream flow condition combinations resulting in x_{shock} (constant for the R4 aerofoil with resulting M_{sh} and C_L values; $Re = 3 \times 10^6$)

α	M_∞	M_{sh}	C_L
−1.0	0.723	1.183	0.823
−0.75	0.718	1.222	0.861
−0.5	0.714	1.271	0.901
−0.25	0.710	1.292	0.937
0	0.705	1.310	0.970[a]
.25	0.701	1.300	1.00
.5	0.697	1.298	1.04
.75	0.695	1.331	1.07
1.0	0.693	1.378	1.10

[a]Original design point.

To separate the effect of x_{shock} movement from the variation of shock strength at off-design conditions, a second study was performed using M_∞ and α combinations that generate a variation of C_L with the same x_{shock} on the clean wing section. Appropriate flow conditions were found by iterating M_∞ for a range of α to obtain the required x_{shock} (all within 2%c of the design point value); the conditions are shown in Table 1 along with an approximate pre-shock Mach number (M_{sh}), calculated using the surface c_p value just upstream of the shock and an assumption of isentropic flow up to that point.

The variation of L/D with C_L for the flow conditions shown in Table 1 is shown in Fig. 19 for the same two- and three-dimensional SCB designs used in Fig. 18. Comparing the off-design performance of two- and three-dimensional SCB designs that produce a similar L/D gain at the design point ($C_L \simeq 0.97$) reveals little difference, except for the highest θ_{ramp} designs (e.g., compare the 2° two-dimensional SCB with the 6° three-dimensional SCB) at low C_L values, where the two-dimensional SCB begins to perform better than the three-dimensional SCB. The performance degradation at observed low C_L is caused by a breakdown of the λ-shock into a double-shock system. This is because the local Mach number just ahead of the shock has been reduced from that at the design point, thus the flowfield is not able to support a triple point at the highest

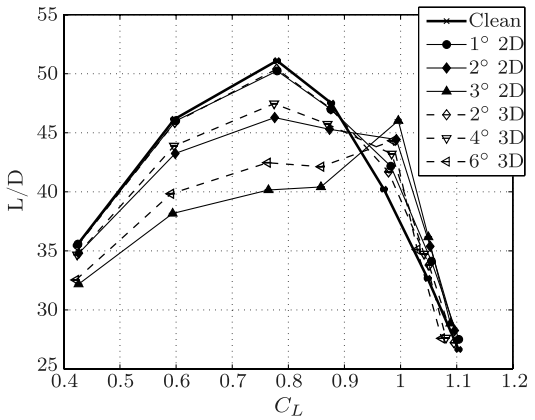

Fig. 18 L/D vs C_L for two- and three-dimensional SCBs with different θ_{ramp} at $M_\infty = 0.705$.

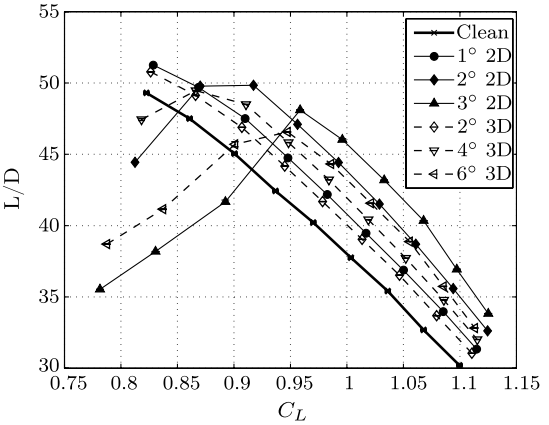

Fig. 19 L/D vs C_L for two- and three-dimensional SCBs with different θ_{ramp} at flow conditions in Table 1.

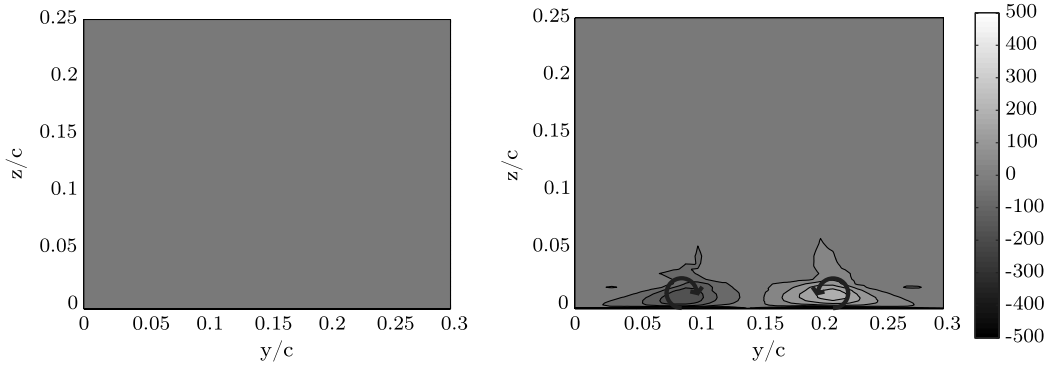

a) 2D SCB with θ_{ramp} = 3º **b) 3D SCB with θ_{ramp} = 6º**

Fig. 20 Contours of ω_{str} on a spanwise plane at $x = 0.9c$.

flow turning angles (the same mechanism causing the sharp drop in L/D as θ_{ramp} is increased beyond $\theta_{ramp,\max L/D}$ in Figs. 8 and 16). The higher flow turning angles required by the three-dimensional SCBs to achieve equivalent design point L/D performance as the two-dimensional designs again leads to the poorer off-design performance at low C_L observed in Fig. 19.

It should be noted that only one family of three-dimensional SCB designs have been analyzed in these studies; it is therefore likely that the off-design performance could be improved; however, it is anticipated that it will still not be able to outperform that of two-dimensional SCBs for the range of operating conditions considered.

F. Vortex Production

One of the reasons behind the continued interest in three-dimensional SCBs is their ability to produce streamwise vortices, and the possibility that this property could lead to improved off-design behavior through suppression of large-scale separation [11–14,17,18]. To visualize vortices, contours of streamwise vorticity were calculated by taking the dot product of the flow vorticity with the local velocity vector, shown in Eq. (1):

$$\omega_{str} = \omega \cdot \frac{\boldsymbol{V}_{xz}}{|\boldsymbol{V}_{xz}|} \tag{1}$$

where $\boldsymbol{V}_{xz}$ is the x-z component of the local velocity vector, defined so as to remove the y component of vorticity, associated with shear in the boundary layer (as this could hinder visualization of the streamwise vortices): $\boldsymbol{V}_{xz} = [V_x, 0, V_z]^T$.

Contours of ω_{str} are compared for typical two- and three-dimensional ($b_{spacing} = 0.3c$, $b_{width} = 0.1c$, and $b_{edge} = 0.02c$) SCBs on a spanwise plane downstream of the SCB in Fig. 20, indicating the presence of a counter-rotating pair of streamwise vortices located downstream of the shoulders of the three-dimensional SCB (see Fig. 20b. Discrepancies between the shape and size of the vortex pair in Fig. 20b are likely to be due to the coarse spanwise mesh spacing ($0.01c$ – see Fig. 4b) relative to the vortex diameter.

These vortices appear to be produced by two opposing spanwise shear flows, driven by spanwise pressure gradients over the SCB. The first is generated at the SCB crest, due to the back leg of the λ-shock being located just downstream of the normal shock location either side of the three-dimensional SCB, as shown in Fig. 10a. This gradient generates a spanwise flow onto the SCB just after the crest, as shown in Fig. 21a. The flow onto the SCB continues to the end of the tail, where it is met by a local region of increased pressure, generated by the concave streamwise geometry of the SCB tail meeting the wing surface (see Fig. 3b). This (small) pressure gradient pushes the boundary layer flow away from the SCB, in the opposite direction to the bulk flow from the crest pressure gradient, as shown in Fig. 21b (the flow off the SCB can just be seen very close to the surface at the shoulders of the SCB). The spanwise shear flows close to the surface over the SCB crest and tail, and pressure gradients that drive them, are also shown in Fig. 22, which gives a planform view of the wing section upper surface with the same SCB as that shown in Fig. 21 (the vertical lines spanning Fig. 22 indicate the location of the measurement planes used in Fig. 21). The flow onto the SCB immediately after the crest can be seen, with the weak flow off the SCB at the tail indicated by a (slight) deviation of the streamlines. The opposing shear flows indicated in Fig. 21 roll up to form the weak streamwise vortices seen in Fig. 20 further downstream. It is also possible that local flow separation around the SCB crest plays a role in vortex production, as noted by Ogawa et al. [13], although this is difficult to assess given the mesh size limitations for these CFD investigations.

To use three-dimensional SCBs for buffet margin improvement, stronger streamwise vortices need to be generated. One way of increasing vortex strength is by increasing the spanwise pressure gradient at the end of the SCB tail, thus increasing the magnitude of the opposing shear flow, which leads to vortex production. This can be achieved by reducing l_{tail}, which, for a given l_{ramp} and θ_{ramp}, increases the angle at which the SCB tail meets the wing surface and,

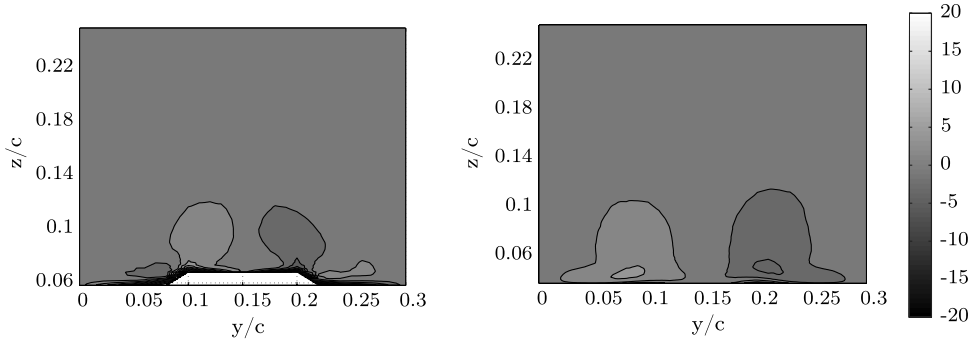

a) Plane at x = 0.5c **b) Plane at x = 0.7c**

Fig. 21 Contours of V_y on spanwise planes over a three-dimensional SCB with $b_{spacing} = 0.3c$, $b_{width} = 0.1c$, $b_{edge} = 0.02c$, and $\theta_{ramp} = 6°$ at design point.

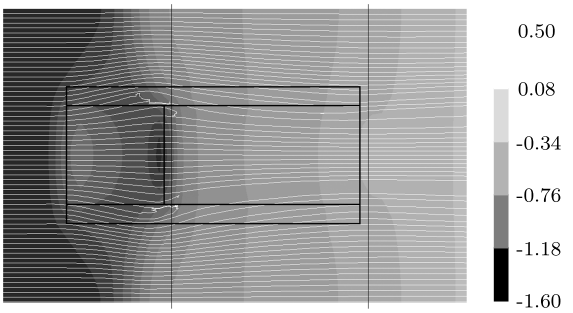

Fig. 22 Upper surface c_p contours and streamlines close to surface on wing section with three-dimensional SCB.

thus, the local streamwise concavity. Figure 23a shows contours of ω_{str} downstream of the SCB tail (the same relative distance downstream to the end of the SCB tail as in Fig. 20b for a three-dimensional SCB of the same design in Fig. 20b, but with l_{tail} half the size. A comparison with Fig. 20b indicates that stronger vortices have indeed been produced in this case.

A second method of increasing the spanwise pressure gradient is to increase θ_{ramp}, which will further reduce the low pressure behind the SCB crest (especially if flow reexpansion starts to occur), as well as increase the pressure at the end of the SCB tail. Figure 23b shows ω_{str} contours on a spanwise plane behind an SCB with the same design as that used in Fig. 20b, but with $\theta_{ramp} = 8°$. Comparison with Fig. 20b shows a gain in both vortex strength and size over the baseline design. The three-dimensional SCB with $\theta_{ramp} = 8°$ has a double-shock rather than λ-shock structure as $\theta_{ramp} > \theta_{ramp,\max L/D}$, and so is likely to experience some level of flow separation behind the SCB crest. This flow separation has been observed to be influential in vortex production by three-dimensional SCBs in previous investigations [12,13], and so this may be a factor in the vortex strength increase observed in Fig. 23b; the same may also be true for the SCB design in Fig. 23a, as the reduced tail length increases the streamwise adverse pressure gradient after the crest, promoting separation.

The relative strength of the vortices produced by these different three-dimensional SCB designs can be quantified by comparing their circulations. These were calculated by an integral of the vorticity through surfaces localized to the approximate vortex shape (based on Figs. 20b and 23) and perpendicular to the vortex path, using Eq. (2):

$$G = \iint_A \omega \cdot \mathrm{d}A \tag{2}$$

The circulation calculations showed large differences in magnitude between the vortices in each pair. These were partly due to the approximated shape and orientation of the integration planes, but mainly due to the coarse spanwise mesh size, as noted previously. As a simple means of quantifying the differences between alternative three-dimensional SCBs, the rms circulation of each counter-rotating pair of vortices was calculated for all three three-dimensional SCB designs by squaring and averaging the circulations for each vortex in the pair and taking the root of the result for each design considered. The results, listed in Table 2, indicate the expected increased circulations associated with the vortices of the designs in Fig. 23, with the greatest value associated with the high θ_{ramp} design shown in Fig. 23b. By repeating the circulation calculations for this high θ_{ramp} design closer to the SCB, and performing a suitable non-dimensionalization, the vortex strength could be compared with those found by Ashill et al. [28] in experimental investigations on sub-boundary-layer vortex generators conducted on transonic aerofoil sections, revealing that the SCB circulation was approximately four times weaker than that of the best performing vortex generators in the study. Although there is likely to be inaccuracy in the vortex prediction, it is clear that the vortices produced by three-dimensional SCBs are still weaker than those of bespoke separation reduction devices such as vortex generators.

G. Buffet Alleviation

The potential for three-dimensional SCBs to reduce large-scale separation and buffet through the production of streamwise vortices has been assessed by looking at various SCB designs over a range of M_∞. The same CFD model and solver settings as the design point studies, detailed in Sec. II.B, were used, with the same number of solution iterations performed for each analysis. The stronger shocks and flow separation associated with these high M_∞ simulations led to a slower solution convergence than that seen for the design point studies; however, the convergence error for the solutions was still very low, with typical differences in L/D values calculated over the last 200 iterations approximately equal to 0.05% of the overall value. Figure 24 compares streamwise τ_{wx} profiles over the clean wing to those over a two-dimensional SCB for several M_∞; negative values of τ_{wx} indicate reversed flow and thus regions of separation. Figure 24a indicates that there is a small separation bubble just after the shock at the design point ($M_\infty = 0.705$); as M_∞ increases, this shock separation bubble grows and trailing edge separation begins, although this is only noticeable in Fig. 24a for $M_\infty \geq 0.73$. At $M_\infty = 0.74$, the separation bubbles have joined, resulting in fully reversed flow from the shock to the trailing edge. This large-scale separation is taken to be indicative of buffet onset [29–31]. Figure 24b shows that the two-dimensional SCB has eliminated shock separation at the design point (due to the breaking up of the shock wave into the λ-shock formation); however, at higher M_∞, flow reexpansion over the SCB crest leads to stronger shocks and larger separation bubbles than the clean wing case. Although the greater separation leads to lower lift values than the clean wing, the λ-shock introduced by the two-dimensional SCB still significantly reduces the wing drag (despite the strengthening of the rear leg of the λ-shock by flow reexpansion), leading to an overall L/D increase for the wing with the two-dimensional SCB for M_∞ from the design point up to the value where full separation is observed behind the shock ($M_\infty = 0.74$ from Fig. 24b).

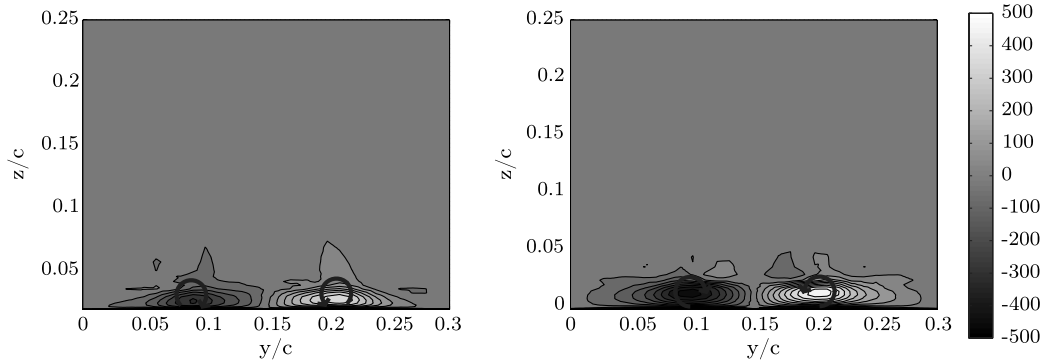

a) Plane at $x = 0.8c$, $l_{tail} = 0.1c$ **b) Plane at $x = 0.9c$, $\theta_{ramp} = 8°$**

Fig. 23 Contours of ω_{str} on spanwise planes over wing section with three-dimensional SCBs at design point.

Table 2 RMS vortex circulation magnitudes from different three-dimensional SCB designs

Three-dimensional SCB design	RMS circulation, m^2/s^a
Baseline (Fig. 20b)	0.1564
$l_{tail} = 0.1c$ (Fig. 23a)	0.2218
$\theta_{ramp} = 8°$ (Fig. 23b)	0.5391

[a]Circulations were calculated $0.12c$ downstream of the end of the SCB tail in each case.

Figure 25 compares τ_{wx} profiles over the wing with a three-dimensional SCB at two spanwise locations for the same M_∞ range used in Fig. 24. Although separation has been greatly increased behind the SCB itself (Fig. 25a), it has been eliminated entirely between the SCBs (Fig. 25b). One cause for the separation pattern observed is that the shock by the SCB crest has been strengthened due to flow reexpansion over the crest, subjecting the local boundary layer to a greater adverse pressure gradient. Moving spanwise away from the SCB crest, the flow reexpansion quickly decays but the compression initiated by the SCB ramp remains (because the SCB crest is close to the shock whereas the SCB leading edge is further upstream), resulting in a λ-shock flow structure between the SCBs with a weak normal shock leg and, thus, a reduced burden on the boundary layer. A further benefit of the three-dimensional shock structure is that the shock location is held more securely for the range of M_∞ than with the two-dimensional SCB (compare Fig. 24b with Fig. 25), which may be beneficial for a wing incorporating the devices.

The second factor determining the separation pattern is the orientation of the streamwise vortices produced by the SCB. At the design point, the vortices produced by the SCB rotate so as to produce a region of downwash behind the SCB itself (see Fig. 20b). However, as M_∞ increases, a secondary set of vortices develop between the original pair, which rotate in the opposite sense, creating a region of upwash. These secondary vortices appear to originate due to a movement of the spanwise pressure gradients around the SCB crest: at M_∞ above the design point, the shock between SCBs moves downstream, simultaneously increasing the size of the high-pressure region on the ramp, pushing flow off the SCB and decreasing the pressure gradient, which is pushing flow onto the SCB just after the crest (compare Fig. 26 with the on-design case in Fig. 10a). This reduction means that the flow off the SCB ramp (generated by the high pressure on the ramp) propagates downstream past the crest, forming a pair of streamwise vortices that are fed by the low-momentum boundary-layer flow being forced onto the SCB tail, as shown in Fig. 27 (compared to the on-design flow in Fig. 21). A similar reversal of vortex rotation was observed when the SCB was moved upstream at the design point, as this is equivalent to moving the shock location downstream relative to the SCB, resulting in a similar modification of spanwise pressure gradients across the SCB crest. The same vortex reversal was observed by Bruce and Babinsky [15] in experimental investigations involving a variable shock location over an SCB on a flat plate. The volume of low-momentum flow being pushed toward the center of the SCB and upward at M_∞ above the design point contributes to the observed large-scale separation in the center of the wing section, although it is difficult to determine the causal relationship between the vortices and separation from these CFD studies.

The separation observed for three-dimensional SCBs is large enough that, despite the attached flow regions between SCBs, the overall lift of the wing section is reduced below that of the clean wing and two-dimensional SCB even at M_∞, where full separation is observed for the latter cases, resulting in lower L/D predictions. This difference in separation levels for the two- and three-dimensional SCBs is highlighted in Fig. 28, which shows flow streamlines on a vertical plane down the SCB centerline at the M_∞ for which full separation was observed for both designs based on Figs. 24b and 25b. The separation behind the shock (located at the SCB crest) for the two-dimensional SCB in Fig. 28a is close to the wing surface,

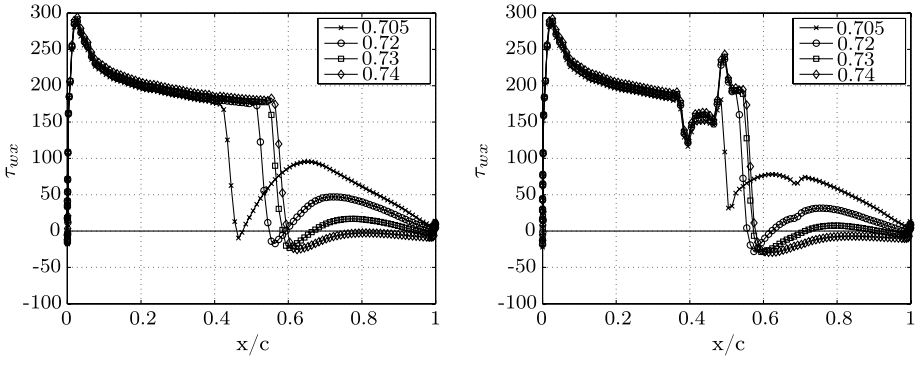

a) Clean wing **b) 2D SCB**

Fig. 24 τ_{wx} profiles for clean wing and two-dimensional SCB at different M_∞ from CFD analysis.

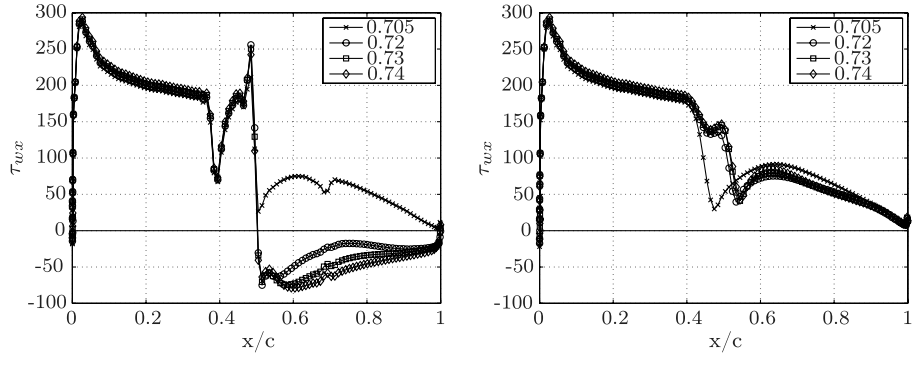

a) Plane down centerline of SCB **b) Plane midway between SCBs**

Fig. 25 τ_{wx} profiles for three-dimensional SCB with $b_{spacing} = 0.3c$, $b_{width} = 0.1c$, $b_{edge} = 0.02c$, and $\theta_{ramp} = 6°$ at different M_∞.

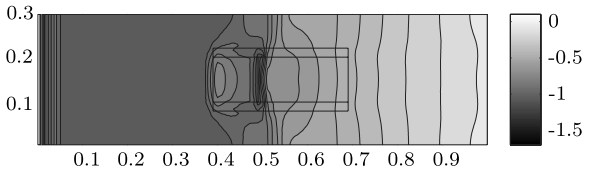

Fig. 26 Upper surface c_p contours at $M_\infty = 0.74$.

whereas a far greater level is observed behind the three-dimensional SCB crest in Fig. 28b, helping to explain the difference in L/D values between the two designs.

The problem with using force predictions for design comparisons at high M_∞ is that Reynolds-averaged Navier-Stokes (RANS) CFD simulations become progressively less accurate as significant levels of flow separation appear, and so improvement to buffet margin was proposed as an alternative measure of off-design performance merit. A wide range of buffet prediction criteria have been proposed [29–33], most of which are based on empirical blends of wind tunnel and flight test data. Some of the more reliable methods are based on prediction of when flow separation reaches a critical stage, often measured experimentally by a divergence of trailing edge pressure [29]. A benefit of CFD simulations is the availability of the wall shear stresses over the entire model surface, which allows the extent of regions of separation to be quantified directly rather than through pressure and wake deviations; in these investigations, a negative value of streamwise (x-direction) wall shear stress, τ_{wx}, was used as a suggestion of reversed flow. As the buffet prediction criteria mentioned previously are based on separation over two-dimensional aerofoils (for three-dimensional wings, an aerofoil section is typically chosen from a separation-prone region of the wing), four different prediction criteria, listed in Table 3, were developed for a wing section with partially separated flow. These criteria are not designed to accurately predict the onset of buffet; rather, they are designed to quantify a potential gain in M_∞ before which large-scale separation takes place and, thus, enable a comparison between alternative SCB designs. M1 is the M_∞ at which the spanwise average of τ_{wx} at $x = 0.9c$ goes to 0, and is thus benefitted by designs exhibiting lower levels of separation and higher shear stresses in regions of attached flow (a measure of a lower shape factor, H, and thus healthier boundary layer). The value $0.9c$ was chosen based on buffet criteria using this location to represent the acceptable limit for separation bubbles [30]. M2 is the M_∞ at which the spanwise extent of reversed flow reaches half the model span, and M3 is the M_∞ at which the whole area of reversed flow reaches 20% of the suction surface area; these are both representative of when separated flow dominates the flow over the wing section. M4 is the M_∞ at which the spanwise average of the incompressible shape factor, H, reaches 2.5, which differentiates separated and unseparated flows, and has been used as a measure for boundary-layer health for experimental three-dimensional SCB studies [12]. The empirical relationships used to develop the buffet onset criteria in Table 3 were largely designed for use on aerofoils and wing sections, which experience separation as a function of chord length, rather than the spanwise variations observed for three-dimensional SCBs; thus, the ability of the criteria to predict the onset of buffet is not known. To assess the accuracy of the criteria for buffet onset prediction would require unsteady RANS simulations of a three-dimensional SCB on the wing section for a range of flow conditions, to identify the point at which shock oscillations begin; these simulations would require a greater mesh resolution and possibly alternative turbulence modeling to be able to capture post-separation flow behavior and boundary-layer re-attachment, which are important features of buffet. In addition, unsteady RANS can require a tuning of α to initiate buffet [34], increasing the number of simulations required for buffet analysis. The increased expense of the computational analysis required for buffet investigations (due to a greater mesh resolution, more expensive turbulence model, and the unsteady simulation itself) and lack of available unsteady experimental data for the wing section used in these studies to validate any potential results prohibited the undertaking of unsteady RANS given the computational resource and time frame limitations for this project. The lack of validation for the criteria in Table 3 means that it cannot be claimed that they define the specific point of buffet onset; rather, they are an indication of separation reduction in critical regions of the wing section at M_∞ in the range where buffet onset is likely. Although they do not therefore provide an absolute measure of buffet onset delay, they are useful for comparing the off-design performance (in terms of separation reduction) between different SCB designs and the clean wing. The use of buffet onset delay, or buffet alleviation in the results presented in the remainder of the paper, is therefore intended as a relative measure of performance improvement under these off-design conditions, rather than a specific measurement of the new buffet onset point.

A series of two- and three-dimensional SCB designs were analyzed over a range of M_∞ to compare buffet onset margins based on the criteria in Table 3. The designs were chosen to provide a range of vortex strengths and separation levels for comparison and are listed in Table 4; all three-dimensional designs have $b_{\text{spacing}} = 0.3c$, $b_{\text{edge}} = 0.02c$ and $l_{\text{ramp}} = 0.1c$, with the baseline design having $b_{\text{width}} = 0.1c$, $\theta_{\text{ramp}} = 6°$, $x_{\text{start}} = 0.39c$, and $l_{\text{tail}} = 0.2c$ with one or more of these values altered between different designs, as noted in Table 4. For each design, M_∞ was varied from 0.67 to 0.77 in intervals of 0.005, holding α constant at the design point value, with all relevant flowfield properties recorded for each design; linear interpolation was used during postprocessing to determine specific values for the buffet onset criteria. Figure 29 plots M1 against M2, M3, and M4, with the Pearson linear correlation coefficients (r) for these three lines as well as all other buffet criteria combinations recorded in Table 5. The high levels of correlation between the criteria suggest that they capture the same trends in separation reduction at high M_∞ and are relatively interchangeable; for the rest of the analysis presented, M1 will be used to assess buffet onset.

To assess the correlation between buffet margin improvement and vortex production, Fig. 30 shows the gain in M1 of the 10 SCB designs over the clean wing case against their design point rms peak vortex strengths (the legend refers to the designs in Table 4). Because

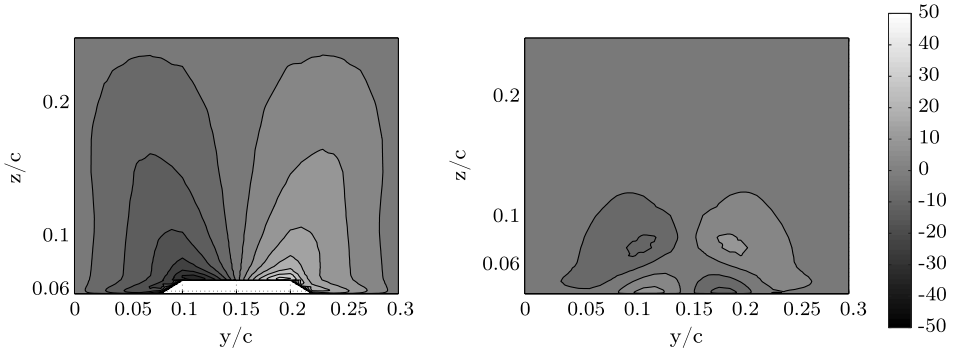

a) Plane at $x = 0.5c$ **b) Plane at $x = 0.7c$**

Fig. 27 Contours of V_y on spanwise planes over a three-dimensional SCB with $b_{\text{spacing}} = 0.3c$, $b_{\text{width}} = 0.1c$, $b_{\text{edge}} = 0.02c$ and $\theta_{\text{ramp}} = 6°$ at $M_\infty = 0.74$.

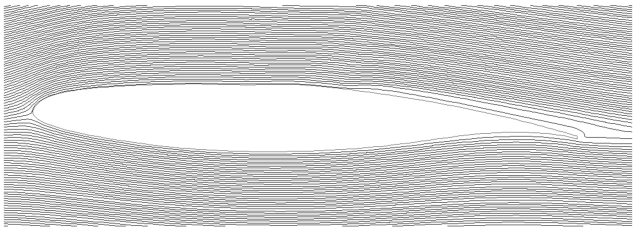

a) 2D SCB

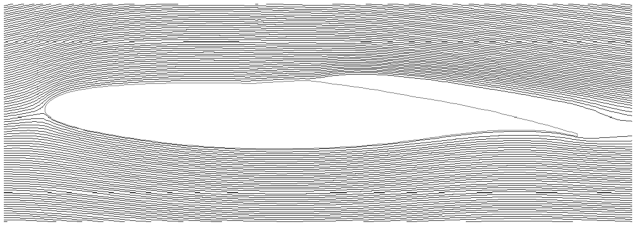

b) 3D SCB

Fig. 28 Streamlines on x-z plane over wing section with SCBs at $M_\infty = 0.74$ located at SCB centerline; flow is left to right.

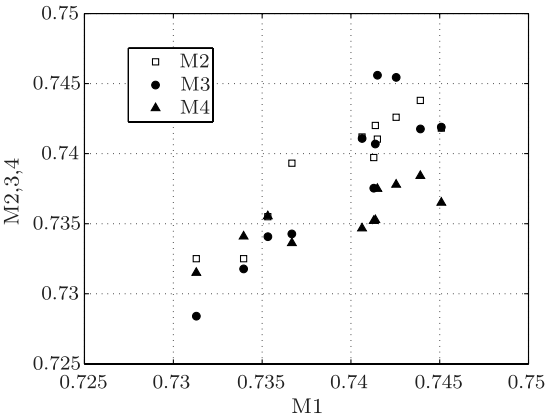

Fig. 29 Correlation of different buffet onset criteria for 11 SCB designs considered.

of the potential inaccuracies in calulation of peak vortex strengths (peak ω_{str}) due to the spanwise mesh resolution mentioned previously, the use of the vortex circulation would have been preferable to compare the strength of vortices between different three-dimensional SCB designs. The problem with circulation calculation is that it requires the determination of bounds for each vortex to define the local plane for integration of vorticity, which vary between the different designs. It was not possible to reliably find the geometric bounds for the vortices using an automated algorithm; the desire to compare the vortex strengths of a large number of SCB designs (those from all the parametric studies undertaken, rather than just from Table 4) made the use of an automated procedure necessary, and thus the peak value of ω_{str}, which was possible to calculate more reliably, was used to compare the vortex strengths. Design point values are a valid metric for comparison because they are closely correlated to off-design vortex strengths, as both on- and off-design vortex strengths are related to the magnitudes of spanwise pressure gradients, which are in turn determined by SCB geometry. It is not clear whether the separation patterns observed at high M_∞ (dictating the buffet boundary) are caused by the vortices or whether they help generate the vortices; however, it is likely that the same physical processes (i.e., spanwise pressure gradients) govern both phenomena, explaining the correlation. For each design, the rms of the peak values of ω_{str} from the two vortex cores were taken at a spanwise plane $0.05c$ downstream of the end of the SCB tail. Taking the ω_{str} measurements at the same streamwise location relative to the SCB allows the strengths of the vortices produced by the SCB to be compared without the losses due to dissipation at a fixed downstream location (due to varying SCB tail ending locations for the different designs). Figure 30 indicates a strong linear correlation between the design point peak ω_{str} and an improvement in the buffet margin, $\Delta M1$ ($r = 0.922$), for the three-dimensional SCB designs (the two-dimensional SCBs are not included in the correlation), as highlighted by the least-squares fit.

Figure 31 compares the variation in L/D gain over the clean wing at the design point with the M1 gain over the clean wing for all SCB designs considered. A Pareto front comprising designs B, D, H, and K is apparent, representing the range of best possible tradeoffs between design point L/D performance and improvements to the buffet margin; the other SCB designs lie close to the front with the exceptions of designs C, G, and J. Designs C and J are versions of the two-dimensional and baseline three-dimensional SCBs with lower values of θ_{ramp}, reducing their on-design L/D performance with no real gain in buffet margin (their performance more closely resembles that of the clean wing; see Fig. 31). Design G was anticipated to delay vortex reversal and flow separation by locating the SCB further downstream than the baseline three-dimensional SCB design (thus becoming optimally located at a higher M_∞); however, the gain in M1 is small and offset by a large drop in on-design L/D due to SCB misalignment with the shock (see Fig. 31).

A final comparison between the two-dimensional and baseline three-dimensional SCBs is shown in Fig. 32, which shows the L/D variation of each design compared to the clean wing, cut off at the predicted buffet onset criterion M1, illustrating the tradeoff between maximizing L/D and extending safe operating range.

Table 3 Wing section buffet criteria

Criterion	Description
M1	M_∞ at which spanwise average of $\tau_{wx,x=0.9c} = 0$
M2	M_∞ at which spanwise extent of $(\tau_{wx,x=0.9c} < 0) = b_{spacing}/2$
M3	M_∞ at which overall area of $(\tau_{wx,x=0.9c} < 0) =$ total area$/5$
M4	M_∞ at which spanwise average of $H_{x=0.9c} = 2.5$

Table 4 SCB designs for buffet analysis

SCB design	Two-dimensional/ three-dimensional	Description
A	Two-dimensional	Clean wing
B	Two-dimensional	$\theta_{ramp} = 3°$
C	Two-dimensional	$\theta_{ramp} = 1°$
D	Three-dimensional	Baseline design
E	Three-dimensional	$b_{width} = 0.06c$, $\theta_{ramp} = 8°$[a]
F	Three-dimensional	$b_{width} = 0.04c$, $\theta_{ramp} = 9°$[a]
G	Three-dimensional	$x_{start} = 0.41c$
H	Three-dimensional	$l_{tail} = 0.1c$
I	Three-dimensional	$l_{tail} = 0.4c$
J	Three-dimensional	$\theta_{ramp} = 3°$
K	Three-dimensional	$\theta_{ramp} = 8°$

[a]θ_{ramp} increased to value giving maximum L/D at design point for comparison with baseline three-dimensional SCB design.

H. Buffet Alleviation Performance Trends

The correlation between buffet margin improvement and design point vortex strength shown in Fig. 30 indicates that, even if the vortices are not solely responsible for the improvement, the same design parameters influence both phenomena. Two key paremeters

Table 5 Buffet criteria Pearson correlation coefficients

	M1	M2	M3	M4
M1	1	0.9359	0.9010	0.8180
M2	0.9359	1	0.8913	0.7552
M3	0.9010	0.8913	1	0.8598
M4	0.8180	0.7552	0.8598	1

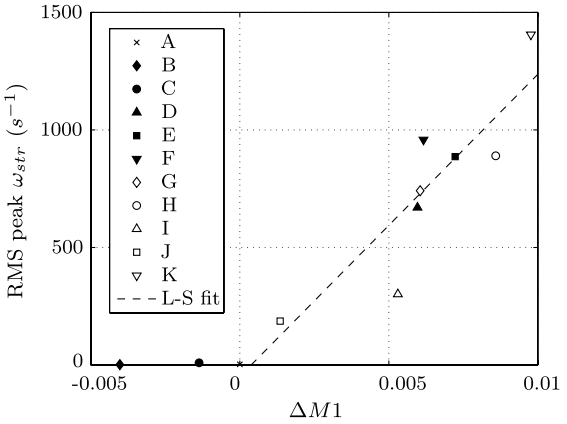

Fig. 30 M1 gain vs on-design rms peak ω_{str} just behind SCB tail.

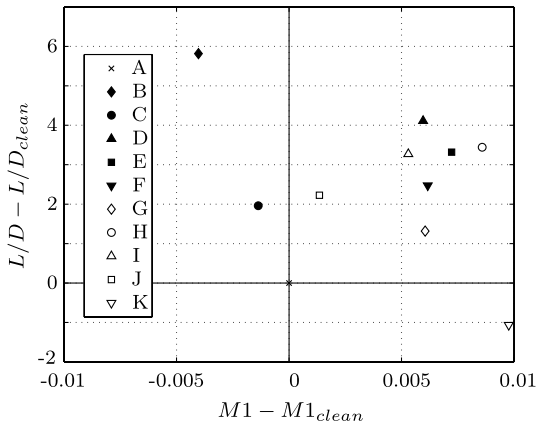

Fig. 31 M1 gain vs on-design L/D gain.

were established previously to be l_{tail} and θ_{ramp} (see Table 3 and Fig. 31), both of which control the spanwise pressure gradients across the SCB. In addition, some variation in buffet margin was also observed for changes to b_{width}; however, for the comparison shown in Fig. 31, these changes were also accompanied by differences in θ_{ramp}, and so the effect could not be isolated. In terms of spanwise pressure gradients, once the SCB is sufficiently isolated (i.e., large enough Φ) to minimize spanwise λ-shock overlap, greater isolation will not increase the gradients any further. However, a greater Φ not only enables larger θ_{ramp} designs to maintain a λ-shock structure on design (maximizing L/D), but reduces the L/D penalty when θ_{ramp} is increased beyond that point, thus allowing a reduced L/D penalty for SCB designs with higher vortex strengths. Increasing Φ should also improve buffet performance by restricting the region of separated flow behind the SCB, although Fig. 31 only indicates small improvements for the higher Φ designs. It is not clear from the results of this limited study how much improvement in buffet margin can be achieved by further increasing θ_{ramp} and Φ, or reducing l_{ramp}, making it difficult to design an SCB with the sole objective of increased buffet margin; such a design would also be likely to have a very poor on-design L/D performance, making it unsuitable for practical use. A far more useful measure of utility is to consider the tradeoff in performance between on-design L/D and increased buffet margin; by substituting buffet margin improvement for design point peak vortex strength just downstream of the SCB tail (possible through the strong correlation seen in Fig. 30), all of the SCB designs considered in the design studies presented earlier in this paper can be compared. The data are presented in Fig. 33, with the Pareto front, which represents the optimal tradeoff between the two objectives, highlighted.

Figure 33 also includes the designs analyzed in the buffet study (detailed in Table 4), the best performing of which lie close to or on the Pareto front. Of these designs, only that with $l_{\text{tail}} = 0.1c$ represents a new point on the Pareto front, indicating that further investigation of this design variable could yield further incremental benefits in terms of buffet alleviation; this is the subject of further research. All the other points on the Pareto front are solely differentiated by θ_{ramp} and their spanwise design variables, and so may be directly compared using these parameters. Figure 34a plots the data points from the Pareto front established in Fig. 33 in terms of the two key design variables Φ and θ_{ramp}, indicating a strong linear correlation ($r = 0.922$). By rotating the coordinate system in the $\Phi - \theta_{\text{ramp}}$ plane to align with the direction of the line of best fit shown in Fig. 34a, the SCB performance variation across the Pareto front can be reduced to a dependence on a single variable (the distance along this line, denoted as x'). Using the linear correlation shown in Fig. 30 to relate peak vortex strength to three-dimensional SCB buffet boundary increase (taking the exact value from Fig. 30 for the two-dimensional SCB), Fig. 34b indicates both L/D and $\Delta M1$ vary linearly with the single combined variable x' ($r = -0.813, 0.882$, respectively). There is a greater spread of results for large values of x' (designs with high $\Delta M1$ and low L/D), which could be due to a more complicated functional relationship governing vortex production, or the large inaccuracies associated with vortex simulation with a coarse grid resolution.

While this dimensionality reduction is useful for this specific design case, it is anticipated that alterations to the design point operating conditions or underlying clean aerofoil design would affect this relationship; thus, this specific combination of these two key variables is unlikely to describe the Pareto front for alternative SCB design problems. Furthermore, the investigation into the effect of other parameters, such as l_{ramp}, l_{tail}, and x_{start}, as well as more detailed SCB designs (i.e., with smoothed edges or variable relative ramp,

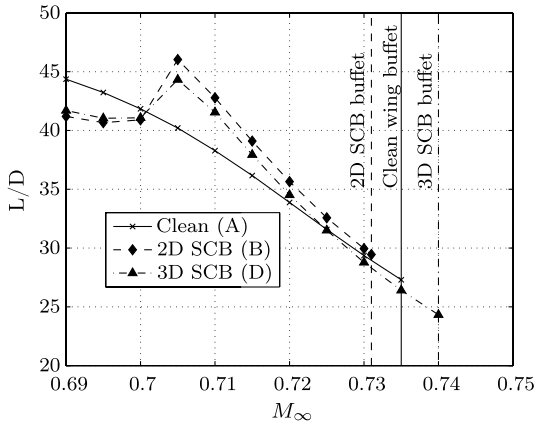

Fig. 32 L/D variation with M_∞ at $\alpha = 0°$.

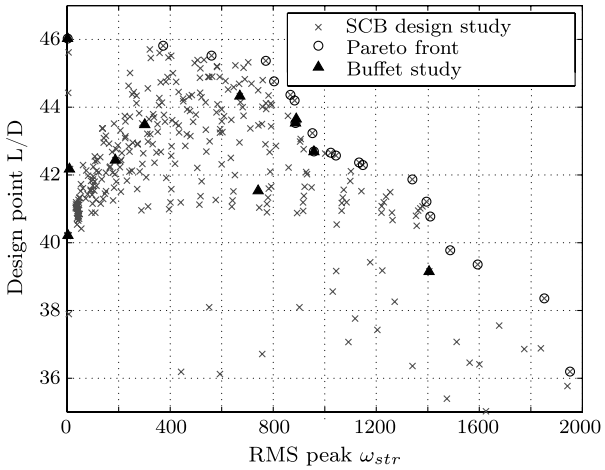

Fig. 33 Design point L/D variation tradeoff with peak vortex strength for all SCB designs.

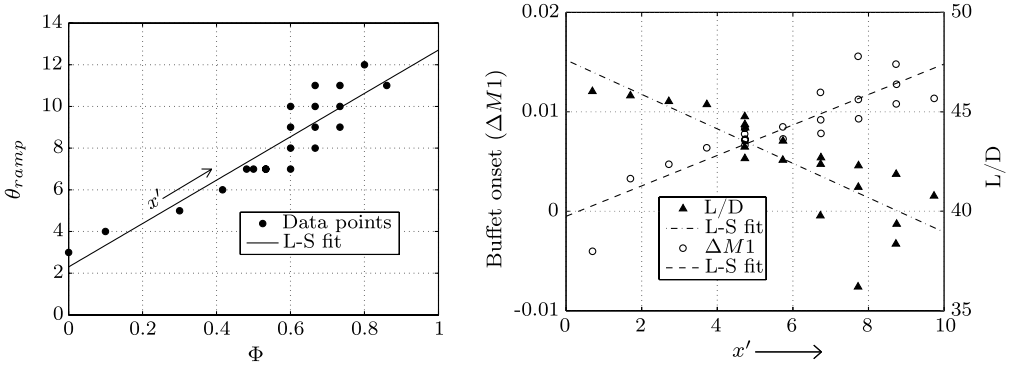

a) Φ and θ_{ramp} variation for points along pareto front

b) Variation of L/D and $\Delta M1$ (interpolated) with single design vector for points along pareto front

Fig. 34 Design variable and objective function variation for data points in Pareto front.

crest, and tail widths) has so far been limited, with Fig. 33 suggesting that possible (incremental) improvements to the Pareto front could be achieved through a more detailed exploration of this higher dimensional design space. These improvements would also alter the ideal design vector established in Fig. 34a, as well as introduce new functional parameter relationships required for Pareto-optimal performance in the higher dimensionality design space.

IV. Conclusions

A numerical investigation into the performance of two- and three-dimensional SCBs on an infinite span turbulent-type transonic wing section under transonic conditions was undertaken. Three key spanwise variables for the SCB (width, spacing, and edge design) were varied in conjunction with the SCB ramp angle (which controls the strength of the shock control device) to assess their effects and inter-dependencies on the wing section performance.

Results of parametric SCB shape modifications indicate that if solely considering design point lift/drag improvement, the extruded two-dimensional SCB design is superior to a three-dimensional SCB array, the former being the limiting case in terms of overlap of three-dimensional λ-shock regions. It is expected that improvements to the three-dimensional SCB performance could be achieved through a wider exploration of the available design space (in terms of the four variables used in the investigations and the fixed streamwise SCB design), as well as improvements to the geometric parameterization in terms of removal of sharp edges to the SCB shoulders and a variation of spanwise design along the SCB length; however, it is anticipated that improvements will not be able to overcome the inherent limitation in achievable L/D improvement that a three-dimensional array has over an extruded two-dimensional device.

The potential advantage of three-dimensional over two-dimensional SCBs has been hypothesized to come through off-design performance gains, including buffet alleviation through the production of streamwise vortices. Counter-rotating streamwise vortex pairs were identified for the three-dimensional SCBs investigated, with the production mechanism linked to opposing shear flows set up by spanwise pressure gradients over the three-dimensional SCB crest and tail. The strength of these vortices was manipulated through variation of SCB geometrical parameters that directly affect the strengths of these pressure gradients, namely, the ramp angle and tail length. The accuracy of vortex strengths was limited by the grid resolution used for the computational model; future investigations with higher fidelity simulations could provide a better representation of the streamwise vortices produced by the devices and any variations in the production mechanism between alternative SCB designs.

Investigation of SCB performance under off-design conditions around the design point showed that the greater θ_{ramp} angles required by three-dimensional SCBs to achieve the same level of design point performance benefit as two-dimensional SCBs lead to a greater level of flow reexpansion over the SCB crest at off-design conditions, hence stonger shocks and poorer performance. To achieve the same level of on-design performance as two-dimensional designs, three-dimensional SCBs have to be closer to their maximum performance design and, accordingly, suffer greater performance degradation off design.

Investigations of several SCBs at high M_∞ showed that three-dimensional designs were capable of breaking up regions of separation behind the shock wave, and holding the shock wave fixed over a range of M_∞. The computational model mesh resolution and turbulence model applied made force predictions of post-separation flow unreliable, and so aerodynamic forces could not be used to compare different SCB designs under these conditions. Instead, the performance benefit was quantified through a buffet margin improvement over the clean wing, derived from empirical criteria as a way of quantifying the potential performance gains near buffet onset through reduction of separation. Although the criteria developed were a useful metric for comparison of high M_∞ performance improvement, the link between their predictions and the actual point of buffet onset for a wing with three-dimensional SCB requires higher resolution, unsteady CFD analysis, and ultimately experimental comparisons to be validated; this is suggested as a useful route for future work. The criteria for buffet alleviation were shown to correlate well with the design point vortex strength, allowing a larger range of SCB designs to be assessed for both design point L/D and buffet margin improvement. These two objectives were shown to be conflicting, allowing a Pareto set of SCB designs, representing the optimal tradeoff between these competing objectives, to emerge. Variance along the front was shown to be governed by both micro- and macroscopic SCB design variables (ramp angle and isolation ratio, respectively). With a suitable combination of these parameters, the emphasis of one performance objective over the other for a specific SCB design could be manipulated, allowing the designer a simple means of generating bespoke SCBs for a range of performance requirements, e.g., to suit different regions of a transonic aircraft wing. The ability to design such a range of SCBs for a real aircraft wing requires an analysis of their performance tradeoff on a more realistic model, incorporating the effects of wing sweep. Future work should therefore focus on the changes to the variable trends and design rules for three-dimensional SCBs achieving an optimal tradeoff between the performance objectives that occur when moving to an infinite swept wing model, and ultimately to a three-dimensional wing.

Acknowledgment

The authors would like to thank the United Kingdom Engineering and Physical Sciences Research Council for funding the research.

References

[1] Tai, T., Huson, G., Hicks, R., and Gregorek, G., "Transonic Characteristics of a Humped Airfoil," *Journal of Aircraft*, Vol. 25, No. 8, 1988, pp. 673–674; also AIAA paper 87-1239, June 1987.

[2] Ashill, P., Fulkner, J., and Shires, A., "A Novel Technique for Controlling Shock Strength of Laminar-Flow Aerofoil Sections," *DGLR Bericht*, Pt. 6, 1992, pp. 175–183.
[3] Sommerer, A., Lutz, T., and Wagner, S., "Numerical Optimisation of Adaptive Transonic Airfoils with Variable Camber," *Proceedings of the 22nd International Congress of the Aeronautical Sciences*, Harrogate, U.K., 2000.
[4] Stanewsky, E., Délery, J., Fulkner, J., and de Matteis, P., "Synopsis of the Project EUROSHOCK II," *Notes on Numerical Fluid Mechanics and Multidisciplinary Design: Drag Reduction by Shock and Boundary Layer Control—Results of the Project EUROSHOCK II*, Vol. 80, Springer-Verlag Berlin Heidelberg, 2002, pp. 1–124.
[5] König, B., Pätzold, M., Lutz, T., and Krämer, E., "Shock Control Bumps on Flexible and Trimmed Transport Aircraft in Transonic Flow," *Notes on Numerical Fluid Mechanics*, Vol. 96, Springer-Verlag Berlin Heidelberg, 2007, pp. 80–87.
[6] Ogawa, H., and Babinsky, H., "Evaluation of Wave Drag Reduction by Flow Control," *Aerospace Science and Technology*, Vol. 10, No. 1, 2006, pp. 1–6.
doi:10.1016/j.ast.2005.08.001
[7] Monner, H., Breitbach, E., Bein, T., and Hanselka, H., "Design Aspects of the Adaptive Wing—The Elastic Trailing Edge and the Local Spoiler Bump," *Aeronautical Journal*, Vol. 104, No. 1032, 2000, pp. 89–95.
[8] Birkemeyer, J., Rosemann, H., and Stanewsky, E., "Shock Control on a Swept Wing," *Aerospace Science and Technology*, Vol. 4, No. 3, 2000, pp. 147–156.
doi:10.1016/S1270-9638(00)00128-0
[9] Kutzbach, M., Lutz, T., and Wagner, S., "Investigations on Shock Control Bumps for Infinite Swept Wings," *Proceedings of the 2nd AIAA Flow Control Conference*, Portland, Oregon, 2004.
[10] Pätzold, M., Lutz, T., Krämer, E., and Wagner, S., "Numerical Optimization of Finite Shock Control Bumps," *44th Aerospace Sciences Meeting and Exhibit*, Reston, VA, AIAA, Paper 2006-1054, 2006.
[11] Holden, H., and Babinsky, H., "Shock/Boundary Layer Interaction Control Using 3D Devices," *41st Aerodspace Sciences Meeting and Exhibit*, Reno, Nevada, AIAA Paper 2003-0447, 2003.
[12] Ogawa, H., *Experimental and Analytical Investigation of Transonic Shock-Wave/Boundary-Layer Interaction Control with Three-Dimensional Bumps*, Ph.D. Thesis, Univ. of Cambridge, Cambridge, U.K., 2006.
[13] Ogawa, H., Babinsky, H., Pätzold, M., and Lutz, T., "Shock-Wave/Boundary-Layer Interaction Control Using Three-Dimensional Bumps for Transonic Wings," *AIAA Journal*, Vol. 46, No. 6, 2008, pp. 1442–1452.
doi:10.2514/1.32049
[14] Wong, W., Qin, N., Sellars, N., Holden, H., and Babinsky, H., "A Combined Experimental and Numerical Study of Flow Structures over Three-Dimensional Shock Control Bumps," *Aerospace Science and Technology*, Vol. 12, No. 6, 2008, pp. 436–447.
doi:10.1016/j.ast.2007.10.011
[15] Bruce, P., and Babinsky, H., "An Experimental Study into the Flow Physics of Three-Dimensional Shock Control Bumps," *Proceedings of the 49th AIAA Aerospace Sciences Meeting*, Orlando, Florida, 2011.
[16] Qin, N., Wong, W., and LeMoigne, A., "Three-Dimensional Contour Bumps for Transonic Wing Drag Reduction," *Proceedings of the Institution of Mechanical Engineers, Part G: Journal of Aerospace Engineering*, Vol. 222, No. 5, 2008, pp. 619–629.
doi:10.1243/09544100JAERO333
[17] König, B., Pätzold, M., Lutz, T., Krämer, E., Rosemann, H., Richter, K., and Uhlemann, H., "Numerical and Experimental Validation of Three-Dimensional Shock Control Bumps," *Journal of Aircraft*, Vol. 46, No. 2, 2009, pp. 675–682.
doi:10.2514/1.41441
[18] Babinsky, H., and Ogawa, H., "SBLI Control for Wings and Inlets," *Shock Waves*, Vol. 18, No. 2, 2008, pp. 89–96.
doi:10.1007/s00193-008-0149-7
[19] Redeker, G., "DLR-F4 Wing Body Configuation," *A Selection of Experimental Test Cases for the Validation of CFD Codes*, Vol. II, AGARD AR 303, Aug. 1994, Chap. B.
[20] Vassberg, J., DeHaan, M., Rivers, S., and Wahls, R., "Development of a Common Research Model for Applied CFD Validation Studies," *26th AIAA Applied Aerodynamics Conference*, Reston, VA, AIAA Paper 2008-6919, Aug. 2008.
[21] Jupp, J., "Interference Effects of the A310 High-Speed Wing Configuration, Subsonic/Transonic Configuration Aerodynamics," AGARD AGARD-CP-285, Neuilly-sur-Seine, France, 1980.
[22] Engineering Sciences Data Unit (ESDU), "Methods for Estimating the Pressure Distribution on a Two-Dimensional Aerofoil in Viscous Transonic Flow," ESDU TR 96028.
[23] FLUENT, Fluent 12.1 User's Guide, ANSYS.
[24] Hutton, A., and Ashworth, R., "The Challenge of Turbulence Modelling in Modern Aeronautical Design," *International Journal for Numerical Methods in Fluids*, Vol. 47, Nos. 8–9, 2005, pp. 721–737.
doi:10.1002/fld.868
[25] Spalart, P., and Allmaras, S., "A One-Equation Turbulence Model for Aerodynamic Flows," *La Recherche aerospatiale : bulletin bimestriel de l'Office national d'etudes et de recherches aerospatiales*, Vol. 1, 1994, pp. 5–21.
[26] Tucker, P., "Introduction: Computational Aerodynamics," *Philosophical Transactions of the Royal Society, A*, Vol. 365, No. A, 2007, pp. 2379–2388.
doi:10.1098/rsta.2007.2014
[27] Jenkins, R. V., Johnson, W. G. Jr., Hill, A. S., Mueller, R., and Redeker, G., "Data from Tests of a R4 Airfoil in the Langley 0.3-Meter Transonic Cryogenic Tunnel," NASA TM 85739, Washington, D.C., 1984.
[28] Ashill, P., Fulkner, J., and Hackett, K., "Research at DERA on Sub Boundary Layer Vortex Generators (SBVGs)," *Proceedings of the 39th AIAA Aerospace Sciences Meeting*, Reno, Nevada, AIAA Paper 2001-0887, 2001.
[29] Pearcey, H., "A Method for the Prediction of the Onset of Buffeting and other Separation Effects from Wind Tunnel Tests on Rigid Models," AGARD Rept. 223, 1958.
[30] Thomas, F., and Redeker, G., "Facilities and Techniques for Aerodynamic Testing at Transonic Speeds and High Reynolds," AGARD CP-83, Gottingen, Germany, 1971.
[31] Engineering Sciences Data Unit (ESDU), "An Introduction to Aircraft Buffet and Buffeting," ESDU TR 87012.
[32] Gadeberg, B., and Ziff, H., "Flight-Determined Buffet Boundaries of Ten Airplanes and Comparisons with Five Buffeting Criteria," National Advisory Committee for Aeronautics (NACA) RM A50127, 1951.
[33] Butkewicz, P., "Buffet Analysis," Nato's Advisory Group for Aerodynamics Research and Development (AGARD) AR 82, 1975.
[34] Deck, S., "Numerical Simulation of Transonic Buffet over a Supercritical Airfoil," *AIAA Journal*, Vol. 43, No. 7, July 2005, pp. 1556–1566.
doi:10.2514/1.9885

S. Fu
Associate Editor